Direct Tablet Formation by Electrospinning and Compaction

by

Nicholas Matti Sondej

B.S. Mechanical Engineering, Georgia Institute of Technology (2012)

Submitted to the Department of Mechanical Engineering
in partial fulfillment of the requirements for the degree of

Master of Science in Mechanical Engineering

at the

MASSACHUSETTS INSTITUTE OF TECHNOLOGY

June 2014

Author ..... Signature redacted .....
Department of Mechanical Engineering
May 9, 2014

Certified by.... Signature redacted .....
Alexander H. Slocum
Pappalardo Professor of Mechanical Engineering
Thesis Supervisor

Signature redacted

Accepted by .....
David E. Hardt
Ralph E. and Eloise F. Cross Professor of Mechanical Engineering
Chairman, Department Committee on Graduate Students

Direct Tablet Formation by Electrospinning and Compaction

by

Nicholas Matti Sondej

Submitted to the Department of Mechanical Engineering
on May 9, 2014, in partial fulfillment of the
requirements for the degree of
Master of Science in Mechanical Engineering

Abstract

A process and physical system were developed to manufacture pharmaceutical tablets through an electrospinning operation and subsequent compaction. Theoretical simulations of the electrospinning were run to predict physical system performance, and a proof-of-concept device was designed, produced and tested. The process was demonstrated to be theoretically scalable to levels of production suitable for industrial pharmaceutical manufacturing. The system demonstrated clear advantages over preexisting pharmaceutical manufacturing equipment, eliminating airborne drug particulate matter, minimizing liquid drying time, and enabling a more agile, liquid-based continuous manufacturing process to be utilized for pharmaceutical production. Future work was specified to refine and optimize the process, and improve process control and monitoring in order to meet the pharmaceutical industry's strict regulatory controls.

Thesis Supervisor: Alexander H. Slocum
Title: Pappalardo Professor of Mechanical Engineering

Acknowledgments

The sum total of my entire MIT experience would not have been possible without the crazy, inspiring, awesome and motivating personality that is of course, Professor Alexander Slocum. I would like to thank Alex for pushing the entire Precision Engineering Research Group (PERG) to think differently and deterministically, to maintain a healthy balance of hard work, intense exercise and good company, and to give us a role model whom we worked hard for, not because we had to, but because he sets the highest bar for himself, and who are we not to attempt the same.

Thank you to Professor Bernhardt Trout for providing a most interesting, applied, industry research problem to work on for the past two years. It was the sort of work I had hoped to be able to do at MIT and your collaboration with Novartis made that possible.

I will always be in awe of the men and women of PERG, whose incredible successes and talents have inspired me to do more, to be more, and to learn more. If I pushed myself harder, it was always to try to catch up to each of you.

Special thanks goes to National Instruments, for their generous donation of NI data acquisition equipment towards the project, as well as to Professor David L. Trumper, of the MIT Precision Motion Control Laboratory, for facilitating communication and the support from National Instruments.

I would especially like to thank Mark Belanger and the Edgerton Center Student Shop; Ken Stone, Hayami Arakawa and Brian Chan and the MIT Hobby Shop, and Pierce Hayward and the AMP Graduate Student Machine Shop for their continual technical support, use of machine shop facilities and endless patience throughout the process.

To my family - thank you for the support throughout this process. It took my attention away from you many times, yet you were always there throughout. Special thanks to Mom, for proof-reading one more paper, with the same mastery of eloquent, concise phrasing as ever.

Leslie, Joan and Una - thank you for being my adopted aunts while at MIT,

making sure I always had enough baked goods, and sending me emails to ensure I didn't starve due to a lack of free food from around campus. It was a pleasure to drop by constantly and brighten your days, and have your never-ceasing support.

Finally, I owe my sanity, good health and energy to the men and women of the MIT Cycling and Triathlon Clubs who provided an outlet and release from the daily office grind with a more physically enjoyable form of delightful punishment.

-Nick

Contents

THIS PAGE INTENTIONALLY LEFT BLANK

List of Figures

THIS PAGE INTENTIONALLY LEFT BLANK

List of Tables

THIS PAGE INTENTIONALLY LEFT BLANK

Chapter 1

Introduction

In recent years, the pharmaceutical industry has begun to focus its research and development efforts on developing more efficient drug manufacturing processes. The impetus for this move is to accelerate the process of developing new drugs, as well as to enable pharmaceutical manufacturing facilities to respond faster to changes in market demand. Pharmaceutical manufacturing agility - the ability to produce pills in a large spectrum of different batch sizes and formulations - has become a significant functional requirement for next-generation processes. The industry seeks to both decrease the facility size and capital costs, and increase the flexibility of future manufacturing equipment. Current research has thus shifted away from the current batch manufacturing schema towards a completely different manufacturing paradigm - continuous manufacturing - which has seen proven success in various other industries.

1.1 Objective

The goal of this research was to develop a continuous manufacturing process for producing pharmaceutical tablets. The design space for this research can be found in Figure 1-1. It required the system to accept, as an input, a viscous, drug-laden polymer solution from pre-existing upstream processes and produce discrete, solid tablets as output.

Additionally, there were several important system functional requirements iden-

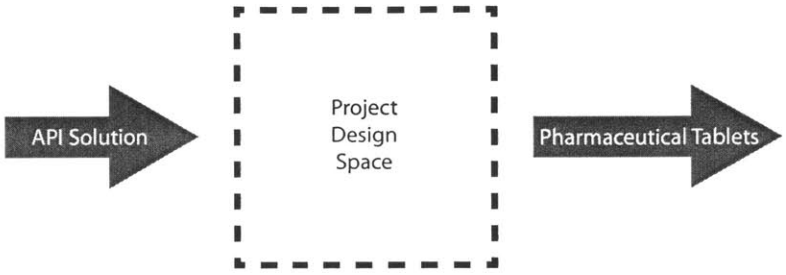

Figure 1-1: High level view of research design space

tified at an early stage in the design process. Table 1.1 displays these requirements, which were developed from analysis of the design space, as well as of the larger overall pharmaceutical manufacturing environment in which the system would perform.

Functional Requirement	Detail
Minimize airborne API particulates	Current powder-based systems produce ambient airborne API particulates which produce a respiratory hazard to workers that the continuous system should reduce
Competitive production rate	Novartis goal production rate is ability to produce 1 billion pills per year
Liquid-based tableting	Upstream processes produce a liquid, polymeric solution from which the tableting system must produce solid, dry pills
Continuous production	System must be able to maintain 24/7 tableting operation with no downtime for duration of weeks at a time

Table 1.1: System functional requirements

1.2 Batch vs. Continuous Manufacturing

Batch production, as it is currently implemented in the pharmaceutical industry, involves numerous, discretized, serial processes, which are detailed by Figure 1-2. The label 'batch production' comes from the fact that individual pills are manufactured in a batch, which must pass entirely through a specific step in the overall process

before the next batch can be sent through. There are often bottlenecks in the batch production paradigm, as certain processes - often drying - take longer than others. This results in an inefficient manufacturing schema, as batches will either accumulate in inventory while waiting for a slower process, or faster processes must be run at reduced rates, wasting manufacturing capability. However, this manufacturing schema has been ingrained in the pharmaceutical industry as the result of a combination of technological momentum and persistence, and a risk-averse regulatory environment which tends to discourage large technological changes.

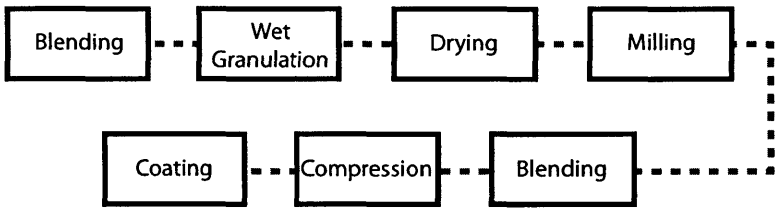

Figure 1-2: Example batch production manufacturing process steps

Batch production is a relatively inflexible manufacturing process, as it is currently implemented in the pharmaceutical industry. It is often used to produced powder-based pharmaceutical tablets - that is, tablets which are produced by filling a die cavity with a powder containing the drug products, and then compressing the powder into a hard, monolithic tablet. The capital equipment involved in such a manufacturing paradigm is generally sized to the desired batch size, with different plants, or at least separate manufacturing lines, required to manufacture drugs of significantly different batch sizes. This is a problem, because a growing trend in the pharmaceutical industry has been towards more user-specific, smaller batch treatments, which the current state of manufacturing technology is ill-equipped to produce cost-effectively.

Continuous manufacturing is defined as a manufacturing process in which a constant supply of inputs to the process - generally raw materials or intermediate components - result in a proportionally constant supply of outputs in the form of finished products and any process waste. The economics of manufacturing theory categorize raw materials, intermediate components, and finished products that are in storage

as inventory, as financial liabilities, since they may depreciate in value over time and generate no income until they are either used in the production of finished goods, or sold. Continuous manufacturing reduces these inefficiencies, since intermediate components are inherently consumed by the manufacturing process at the same rate as they are created, and since there is a finer degree of control over production rate with a continuous system. Indeed, continuous manufacturing allows for much flexibility in adjusting production rate to market demand - any required changes in production rate can be implemented in the time it takes one pill to pass entirely through the manufacturing system. This offers a much faster response time than batch manufacture, where production rate changes can only be made after the entire current batch goes through the system. Additionally, since continuous manufacturing requires a constant flow of materials through the system, a liquid-based system becomes more appropriate as compared to current powder-based technology.

1.3 Continuous Fiber Production

A significant proportion of both current and future pharmaceutical manufacturing time is dedicated to drying liquid solutions into solid products. In batch production, the entire pharmaceutical batch is dried at once and subsequent processes simply wait on the drying step to complete. Drying time becomes a much more important variable in continuous production, because the entire manufacturing process occurs simultaneously in serial and can only run as quickly as drying can be accomplished. Thus, a process to rapidly dry a continuous solid product from a viscous liquid precursor is desired. Inspiration was drawn from various spinning processes in the synthetic fiber industry, with electrospinnning chosen as the best suited process for the pharmaceutical industry.

Continuous production of polymer products has already been achieved in the synthetic fiber industry through a variety of processes, including melt spinning, wet spinning, and electrospinning. Melt spinning is widely used to produce artificial fibers for use in nylon and other synthetic fabrics. The process, which is illustrated in

Figure 1-3, involves heating a thermoplastic polymer beyond its melting point, then extruding the liquid melt through a plate with numerous orifices to form a shower of small diameter liquid streams.

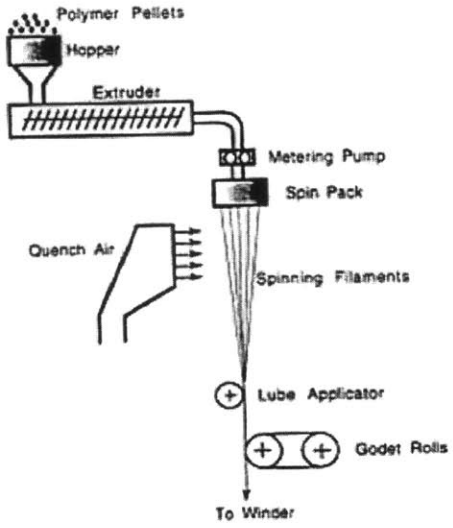

Figure 1-3: Melt spinning production process detail, image courtesy of Textile Knowledge Innovation Platform

The self-weight of the streams causes a stretching that elongates the fibers in the axial direction and reduces their diameter. As the streams are passed through a chamber of cooling gas, the increased surface area to volume ratio as well as decreased mass per unit length of stream allows the stream to quickly cool and form a thin fiber. The melt spinning process is extremely efficient and can be used for high-throughput fiber production, but the temperature increase necessary for the process can damage certain heat-sensitive active pharmaceutical ingredients (API). Additionally the equipment needed for melt spinning can span several stories of a building, in order to provide sufficient height to fully cool and solidify the resultant fibers.

A more compact process with similar physical characteristics and results, but without the API-damaging heating of melt spinning, is electrospinning. The electrospinning process involves the controlled jetting of one or many dry micro- or nanoscale fibers from an electrically charged, liquid solution of dissolved material and its

solvent, under the influence of a high-voltage electric field. Electrospinning is attractive as a continuous manufacturing process to the pharmaceutical industry due to several key characteristics of the process that fulfill several currently unmet needs in the industry. The solvent used to liquefy the fiber material can be fully evaporated in a distance on the order of 300 mm, instead of a few stories, shrinking the manufacturing equipment size. The electrostatic attraction of the charged API and polymer solution to a grounded collector ensures a near-complete delivery of drug product from spinneret to end destination. This allows both precise delivery of API-laden fibers to a desired spatial location, as well as minimizing the amount of airborne pharmaceutical particulate matter present in the manufacturing environment. Environmental pharmaceutical dust is a health hazard for workers in pharmaceutical manufacturing plants, and new manufacturing processes are sought which reduce worker exposure to airborne particulates containing APIs.

1.4 Single Needle Electrospinning

Single needle electrospinning is one of the simplest electrospinning processes. In a single needle setup, spinning solution is pumped through a single conductive needle charged to a high voltage at a measured flowrate. The process is illustrated in Figure 1-4.

The needle is fixtured at a specified distance from a grounded metal collector. As pressure is applied to a fluid reservoir coupled to the needle, a droplet forms on the tip of the needle. The droplet is subject to opposing forces including surface tension, which adheres the droplet to the tip of the needle, and electrostatic force and gravity, in the case of a vertically-oriented system, which pull the droplet downwards towards the collector. If the electrode voltage were to be increased gradually from zero, the droplet can be observed to deform into a characteristic Taylor cone, after Geoffrey Taylor. A Taylor cone, with labeled forces, can be found in Figure 1-5.

At a critical electrode voltage, surface tension forces are overcome by electrostatic forces and a liquid jet will emit from the droplet formed at the tip of the needle. This

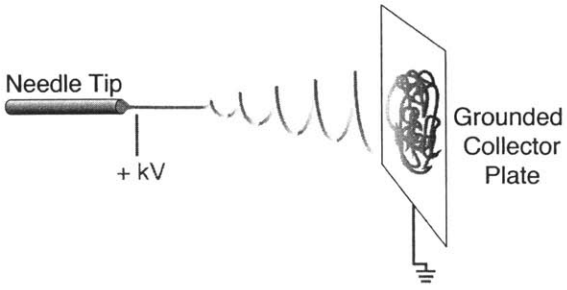

Figure 1-4: Generalized single needle electrospinning setup

jet carries the liquid solution away from the needle tip at a flow rate governed by the process parameters, which will be discussed in more detail later on.

There are three operating modes in which the electrospinning process can proceed. If the flow rate pumped through the needle is equal to the flow rate of solution carried away through the jetting process, electrospinning is carried out at steady state. This equal flow rate situation is considered the optimum operating regime for continuous manufacturing, because it ensures production of consistent fibers, a critical functional requirement of any pharmaceutical manufacturing process. At an operating voltage greater than the critical voltage, if the flow rate of solution supplied is less than the flow rate of solution jetted, the droplet will decrease in size. The Taylor cone from which jetting occurs may actually ascend into the barrel of the needle in this operating regime. This operating regime is considered marginally acceptable, since it will result in the production of fibers, but it is sub-optimal because of the lower production rate and the potential inability to visually monitor the Taylor cone. Machine vision is a proposed mechanism for efficient process monitoring, but it cannot be used in this operating regime. The third operating mode results from a pumped flow rate higher than that of the jetting capacity of a particular equipment setup and results in an oscillation between brief moments of spinning combined with frequent dripping of

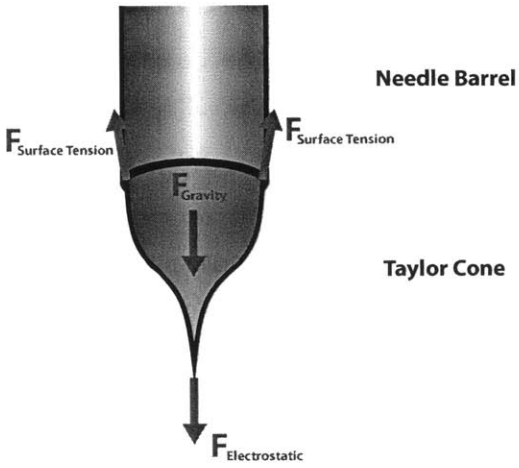

Figure 1-5: Characteristic Taylor cone with labeled forces

large droplets that do not dry before hitting the collector.

Chapter 2

Theoretical Work

2.1 Background

The goal of analysis work on this research was to validate assumptions about the nature of the electrospinning phenomena that the system was based on, in addition to developing virtual prototyping and forecasting tools to quickly iterate through potential designs. The models were used to ensure that physical experiment failures and successes could be used to make informed conclusions. Additionally, process calculations allowed the prototype system to be sized correctly and inferences to be drawn concerning the future scalability of the process to full-scale industrial manufacturing.

Initial work focused on spinneret designs, and the accompanying modeling work focused on fundamental physics at the nozzle tip. Characterization research on nozzle design, multi-needle arraying, and the physics of droplet formation on surfaces was performed, all of which can be found in Appendix A. It was discovered that spinneret optimization had an insignificant effect on fiber spinning performance, but the tools developed for this first phase, such as the electrostatic field finite difference solver described later in this chapter were flexible enough to be adapted for use in later phases.

The next logical research focus was designing a collector which would encourage preferential fiber deposition inside a pill die cavity. While there was some demonstrable success at focusing the electrospun fibers, efforts to deposit the fibers precisely

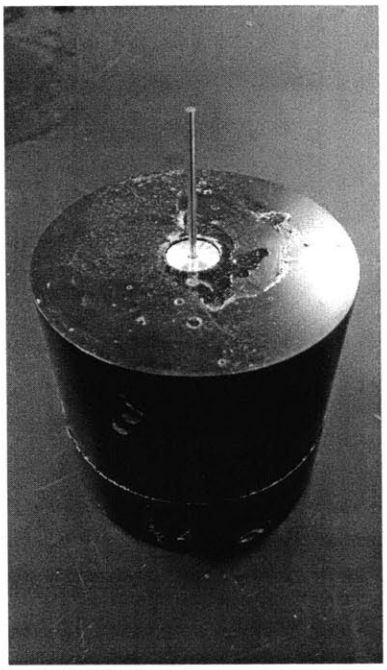

Figure 2-1: 'Lightning rod' style vertical rod collector

into the die cavity failed. The significant obstacle in this phase was producing electric fields which could force the electrospun fibers to concentrate in tight formation along a central axis in order to enter a small orifice. The electric field modeling tools developed previously were used to size the diameter, location and applied voltage of additional field-shaping electrodes designed to focus spun fibers towards the die orifice. A vertical rod collector sticking out of the die, detailed in Figure 2-1, had the most promising performance, but still fell short of the functionality desired.

The results of the 'lightning rod' style collector did build a foundation for the design of the final system configuration, as it was the first example of a collector that could translate through the pill die and provide enough clearance between the walls of the die and the collector for deposited fiber material trapped by the rod. Additionally, this collector design demonstrated that conducting surface areas were gradually insulated by the deposition of spun fibers, since the ability of the collector to entrap fiber material became worse as more fiber was deposited.

2.2 Significant Parameters

The electrospinning process was discovered over 100 years ago, and in more contemporary times has been studied extensively since Taylor published his initial models of electrically-driven jets in 1969 [9]. Subsequent research [3], [7], [8] has identified the following parameters which have varying demonstrable effects on the electrospinning process, in no order of significance:

- Applied electrode voltage
- Spinneret to collector (SC) gap distance
- Solution volumetric flow rate
- Solution dielectric constant
- Solution viscosity
- Ambient temperature
- Ambient relative humidity
- Collector geometry

Solution and environment parameters were controlled by utilizing a constant solution formulation, and by running blocks of experiments on the same day. This was done because environmental parameters were not found to significantly affect experimental results on an experiment to experiment basis, and literature [2] had shown that electrospinning of a large variety of solutions was possible. Controlling for the above variables resulted in a set of four process parameters from which to design experiments:

- Applied electrode voltage
- Spinneret to collector spacing distance
- Solution volumetric flow rate
- Collector geometry

2.3 Electric Field Approximations

The thin jets of spinning solution emitting from the spinneret head are electrically charged, and as such, electrostatic fields significantly influence their trajectories. Electrostatic fields which guide spun fibers towards the collector are thus preferential. A finite difference (FD) solver was written in MATLAB to aid design visualization of the electrostatic fields generated by the experimental setups. The code can be found in Appendix B. The solver allows rapid virtual prototyping of different collector and electrode designs and quickly displays the electrostatic fields which will be generated by the modeled configuration.

Electrostatic theory offers four basic field approximations applicable to potential embodiments of this electrospinning system with which to validate the FD solver, as shown in Figures 2-2(a), 2-2(b), 2-2(c) and 2-2(d).

Initial work to characterize the performance of different spinneret designs used a large 300 mm x 300 mm aluminum plate as a collector, a length scale which was significantly larger than the spinneret, which had a characteristic length on the order of 25 mm or less. With such a small characteristic length, especially in comparison to the spinneret-collector (SC) distance ranges of similar published research [3], [5], [10] of 150-400mm, these setups could be approximated by a point-plate configuration, as seen in Figure 2-2(b).

The final, horizontal rod design is a hybrid of two of these approximations. Viewed down the axial direction of the collector rod, the field lines are approximated by a point-point configuration as seen in Figure 2-2(d). If the final system is viewed from a transverse direction, with the full length of the collector rod in view, the electrostatic fields appear as in Figure 2-2(b).

The actual FD solver builds an array of equations, defined by the matrix:

$$\mathbf{A}\Phi = \mathbf{b} \tag{2.1}$$

where $\mathbf{A}$ is a $(Z \cdot R)$ x $(Z \cdot R)$ coefficients matrix, where Z is the number of nodes in the z-direction and R is the number of nodes in the r-direction, Φ is a column vector

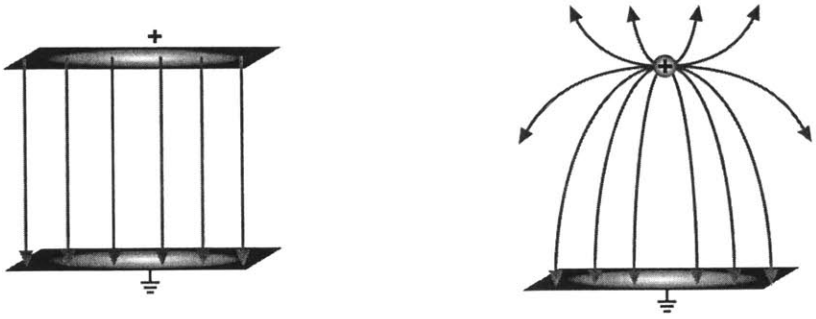

(a) Plate-Plate

(b) Point-Plate

(c) Plate-Point

(d) Point-Point

Figure 2-2: Applicable electrode-collector configurations for electric field approximations

of the unknown electrostatic potentials at each node and **b** is a column vector of constants, which is equal to specific voltages at the boundary nodes of known voltage, and zero everywhere else. The solver first fills the coefficients matrix and constants column vector and then solves for the potentials in Φ using matrix manipulation in MATLAB.

Populating the matrices for subsequent calculation involved creating a mesh of nodes at different spatial points in a virtual representation of the experiment geometry and treating them as surrounded by differential elements. A typical interior node, that is, a node which did not lay on the control volume boundary, can be seen in Figure 2.3.

As can be seen in Figure 2.3, as the finite difference analysis is in progress, a control volume was defined around the current node, $N_{z,r}$, which is the central node

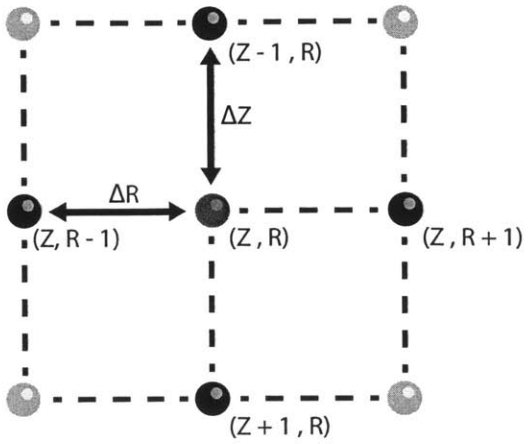

Figure 2-3: Typical arrangement of interior node used in finite difference analysis

in the figure. The voltage at this, and each node was calculated using Gauss' Law (2.2):

$$\nabla \cdot \mathbf{E} = \frac{\rho}{\epsilon_0} \tag{2.2}$$

where $\mathbf{E}$ is the electric field vector, ρ is the total charge density inside the control volume in question and ϵ_0 is the permittivity of free space, or electric constant of the material contained in the control volume, in this case, air. Since all charge in the system, which includes by definition both the charge on the electrified spinneret head, and the lack of charge on the grounded collector, lies on the boundary of the control volume, $\rho = 0$ and thus (2.2) reduces to the Laplace equation (2.3):

$$\nabla \cdot \mathbf{E} = 0 \tag{2.3}$$

In the case of the rectangular mesh in the FD solver, this equation signifies that the sum of the derivative of the electric field with respect to both the radial and axial directions is zero. Thus, no electric field can be 'stored' in the control volume and all electric fields generated by voltage differences between the current node and its neighbors must sum to zero:

$$E_{z-1,r} + E_{z,r+1} + E_{z+1,r} + E_{z,r-1} = 0 \tag{2.4}$$

In short, (2.4) states that all fields that enter the differential element must also leave it. The electric field created between two different electrostatic potentials is:

$$\mathbf{E} = -\nabla \cdot \Phi = -(\frac{\partial \Phi}{\partial z} + \frac{\partial \Phi}{\partial r}) \tag{2.5}$$

where Φ is the electrostatic potential, which is a scalar field defined at each node point. Equation (2.5) enables the calculation of all four of the electric fields created by the voltage differences between the current node, and its neighbors. The FD solver approximates the partial derivatives found in (2.5) by using the definition of the derivative:

$$\frac{\partial \Phi}{\partial z} \approx \frac{\Phi|_{z+\Delta z} - \Phi|_z}{\Delta z} \tag{2.6}$$

Substituting (2.6) and (2.5) into (2.4) yields the governing FD equation for an interior node:

$$\frac{\Phi_{z-1,r} - \Phi_{z,r}}{\Delta z} + \frac{\Phi_{z,r+1} - \Phi_{z,r}}{\Delta r} + \frac{\Phi_{z+1,r} - \Phi_{z,r}}{\Delta z} + \frac{\Phi_{z,r-1} - \Phi_{z,r}}{\Delta r} = 0 \tag{2.7}$$

Equation (2.7) simplifies into:

$$\Delta r \Phi_{z-1,r} + \Delta z \Phi_{z,r+1} + \Delta r \Phi_{z+1,r} + \Delta z \Phi_{z,r-1} + \Phi_{z,r}(-2\Delta z - 2\Delta r) = 0 \tag{2.8}$$

which allows the **A** and **b** matrices of (2.1) to be populated in the FD code.

Boundary Conditions

In the analysis, the boundary conditions for the spinneret and the collector were known, while those at the edges of the control volume were chosen to strike a balance between accuracy and rapid calculation, since the electrostatic effects near the edge

of the control volume were not important to the performance of the system. The boundary nodes which fell on either the spinneret head or the collector were specified with either the experiment voltage or ground respectively, while the field was assumed to be constant, $\nabla\Phi = 0$ at the other boundaries.

2.3.1 Performance

The first simulations replicated the theoretical field line configurations of Figure 2.3 in order to validate the code's functionality. The results from these initial simulations were satisfactory, as an example point-plate simulation in Figure 2-4.

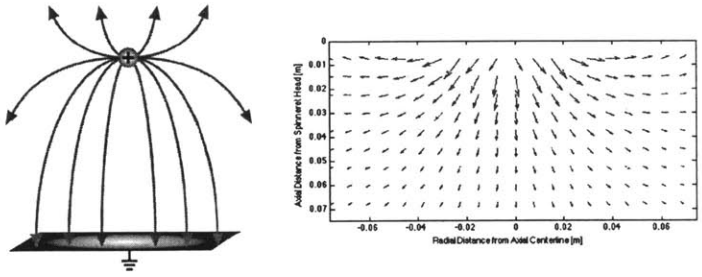

Figure 2-4: Comparison of theoretical field approximation (left) to simulation (right)

Once developed and validated, the FD code was then used to simulate the variation of different experimental parameters, such as the spinneret-collector gap distance, applied spinneret voltage, collector rod diameter, and the effects of additional ring electrodes to test their potential influence on the generated electric fields.

2.4 Electric Field Interference

The system developed in this research is meant to be implemented as a single cell in an array of parallel modules in a manufacturing setup. As the electrospinning setup is static, there is no risk of mechanical interference between each module in a parallel manufacturing scheme. Electrostatic interference is a potential issue when running multiple cells together, if the modules are spaced too closely. This can result in adverse effects in all modules, or inconsistent spinning in the modules at either end

of a linear array of modules, due to edge effects. As was mentioned previously, the spinneret needles can be modeled as point charges, the electric field between which is described by Coulomb's Law as:

$$\hat{E} = (\frac{Q}{-4\pi\epsilon_0}\frac{\hat{r}}{|r|^2}) \tag{2.9}$$

Where $\hat{E}$ is the vector field of electric field strength, Q is the charge on the point charge, ϵ_0 is the electric permittivity of free space, $\hat{r}$ is the unit vector from the charge in the direction of the point at which the field strength is being measured, and $|r|$ is the magnitude of the distance from the charge to the point in space where the electric field strength is being measured. Most importantly, it can be observed from Equation 2.9 that electric field strength decays as a function of $1/|r|^2$ from the charge which is generating the field. With this in mind, at a distance of 300 mm horizontally from the spinneret, which is the typical SC distance, the electric field is 1/9000 of that at the spinneret, so a design which spaces modules at roughly the same length scale as the SC distance should produce minimal electrical interference. This assumption is later tested when performing electrospinning runs with two spinnerets in the final horizontal collector rod design.

2.5 Electric Breakdown Voltage, Ventilation, and Safety

There are significant safety concerns that accompany the generation of a high voltage electrode in an enclosure filled with evaporated volatile organic compounds. The electric breakdown voltage - the voltage at which electrical arcing will occur, and ignition is possible - in ambient air was first calculated to ensure that experiments never positioned the spinneret closer to the collector than a distance equal to three times the electric breakdown distance of air at 50 kV, the maximum voltage that the experimental power supply could provide. The calculation starts with an assumption of a uniform field, such as that between two parallel plates. While this is not an

accurate physical representation of a system with a needle spinneret and a collector, any electrical arcing will occur along the centerline of the setup, where the electrode and collector are closest. Along this centerline, the fields are equivalent for a parallel plate setup and a point and plate setup, so the assumption is valid. The uniform electric field between two parallel plates is represented by Equation 2.10:

$$E = \frac{V}{d} \tag{2.10}$$

Where E is the electric field strength, V is the applied voltage and d is the distance between the spinneret and collector (SC distance). The critical electric field at which point breakdown will occur in air, E_c, is roughly 3 kV/mm [4]. The minimum safe SC distance is desired so Equation 2.10 is first solved for the distance between the two, at the maximum voltage which the power supply can provide:

$$d_{min} = \frac{V_{max}}{E_c} \tag{2.11}$$

Where d_{min} is the minimum safe SC distance and V_{max} is the maximum possible applied voltage. Substituting the known values leaves:

$$d_{min} = \frac{50 \text{ kV}}{3 \text{ kV/mm}} = 16.7\text{mm} \tag{2.12}$$

Since this calculation was based upon an assumed model with a safety factor of one, and the breakdown distance can be affected by humidity and other factors, a safety factor of three was chosen. Thus a SC distance of greater than 51 mm will prevent electrical breakdown. Since the typical SC distance was 300 mm, this was well within a safe region.

Proper ventilation of the experiment enclosure was also important. The enclosure was a 0.6m x 0.6 m x 0.9 m (2 ft x 2 ft x 3 ft nominal) box made from cast acrylic sheets, for a total volume of 0.324 m^3 (12 ft^3 nominal). The box was attached to building ventilation which removed 1.13 m^3/min (40 cfm nominal) of atmosphere from the enclosure. Thus the air handling system was replacing the air in the enclosure over three times per minute, while an amount of ethanol solvent several orders of

magnitude smaller than the volume of the enclosure was added to the enclosure per minute.

2.6 Manufacturing Considerations

The ultimate goal of this electrospinning research is to produce a new system and manufacturing process for use in pharmaceutical production. Although the primary aim of this work was to produce a single functional cell, specifications were also developed for the full system in which it would be a component. Novartis specified that a proof-of-concept system must be scalable to a production rate of 1 billion pills per year. A series of spreadsheets was developed to produce these process calculations and the MATLAB code used to generate some of the following graphs can be found in Appendix D. The first milestone in this process was to identify the high level parameters which would result in the system meeting this functional production goal. The overall production rate of the electrospinning process, and subsequent design of individual cells, is governed by two variables: the mass flow rate of solution through each module, and the number of modules spinning in parallel, and is given as

$$\dot{m}_{\text{api,total}} = N_{\text{modules}} \cdot \dot{m}_{\text{api,module}} \tag{2.13}$$

Where N_{modules} is the number of modules in parallel, $\dot{m}_{\text{api,total}}$ is the overall active pharmaceutical ingredient (API) production rate in [g/hr] and $\dot{m}_{\text{api,module}}$ is the API mass flow rate per module.

At a prescribed total API production rate, Equation 2.13 produces a manufacturing isoperformal curve at the given rate. This curve describes all pairs of parameters which will result in the system meeting the specific target production rate. This isoperformal curve is displayed in Figure 2-5. It allows the number of modules in parallel, or the flow rate per module to be chosen, with the isoperformal curve then specifying the value of the other variable in order to exactly hit the production rate goal. Since the module flow rate will be a parameter in experimental testing, and will be more adjustable than the number of modules in the final system, it will be

considered the independent variable when deriving the equation for this curve.

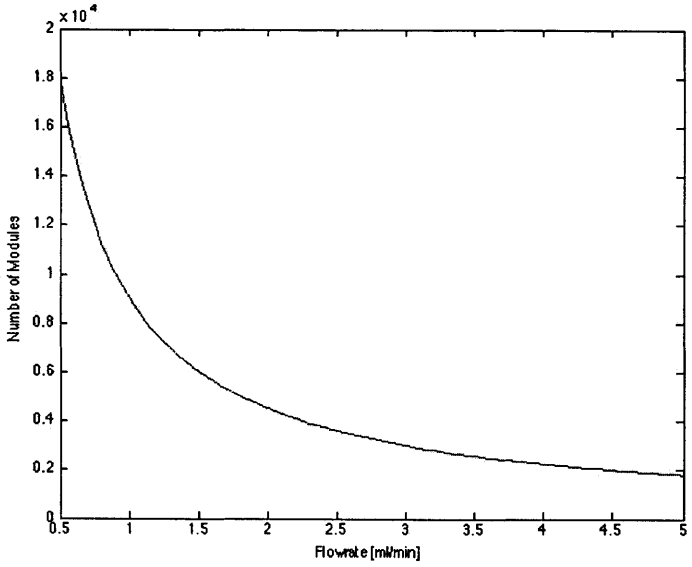

Figure 2-5: Isoperformal curve of production at specified 1 billion pill/year production rate

Starting with the characteristic system equation, Equation 2.13 can be rearranged to solve for the number of modules required:

$$N_{\text{modules}} = \frac{\dot{m}_{\text{api,total}}}{\dot{m}_{\text{api,module}}} \tag{2.14}$$

The total specified API flow rate, $\dot{m}_{\text{api,total}}$ is known, but the API mass flow rate per module must be solved for. Fortunately this can be determined from the total volumetric liquid flow rate per module, which is also known. The API mass flow rate is

$$\dot{m}_{\text{api,module}} = \dot{m}_{\text{module}} \cdot w_{\text{api}} \tag{2.15}$$

Where $\dot{m}_{\text{module}}$ is the total mass flow rate of liquid emanating from each module and w_{api} is the weight percent of API in the solution being spun. The total module mass flow rate can be determined from the total module volumetric flow rate

$$\dot{m}_{\text{module}} = \dot{Q}_{\text{module}} \cdot \rho_{solution} \tag{2.16}$$

Where $\dot{Q}_{\text{module}}$ is the volumetric flow rate of the entire module, a specified parameter, and $\rho_{solution}$ is the density of the entire solution before solvent evaporation. The density of polymer solutions may depend on the enthalpy of mixing of the solution constituents. However, as a simple approximation, a simpler method will be used to approximate the solution density by weighting the individual densities of the solution constituents by their weight percent as follows

$$w_{\text{constituent}} = \frac{m_{\text{constituent}}}{m_{\text{solution}}} \tag{2.17}$$

$$w_{\text{constituent}} \cdot \rho_{\text{constituent}} = \frac{m_{\text{constituent}}}{m_{\text{solution}}} \cdot \rho_{\text{constituent}} = \frac{V_{\text{constituent}}}{m_{\text{solution}}} \tag{2.18}$$

$$\frac{V_{\text{api}}}{m_{\text{solution}}} + \frac{V_{\text{polymer}}}{m_{\text{solution}}} + \frac{V_{\text{solvent}}}{m_{\text{solution}}} = \frac{1}{m_{\text{solution}}} \cdot (V_{\text{api}} + V_{\text{polymer}} + V_{\text{solvent}}) = \frac{V_{\text{solution}}}{m_{\text{solution}}} \tag{2.19}$$

$$\rho_{\text{solution}} = \frac{m_{\text{solution}}}{V_{\text{solution}}} = \frac{1}{(w_{\text{api}} \cdot \rho_{\text{api}} + w_{\text{polymer}} \cdot \rho_{\text{polymer}} + w_{\text{solvent}} \cdot \rho_{\text{solvent}})} \tag{2.20}$$

Substituting Equations 2.15, 2.16, and 2.17 into the rearranged characteristic system equation, Equation 2.14 yields the governing equation for the isoperformal curve:

$$N_{\text{modules}} = \frac{\dot{m}_{\text{api,total}}}{\dot{Q}_{\text{api}} \cdot w_{\text{api}}} \cdot (w_{\text{api}} \cdot \rho_{\text{api}} + w_{\text{polymer}} \cdot \rho_{\text{polymer}} + w_{\text{solvent}} \cdot \rho_{\text{solvent}}) \tag{2.21}$$

THIS PAGE INTENTIONALLY LEFT BLANK

Chapter 3

Experimental Setup

The experimental setup was designed to be a prototype of a single pharmaceutical pill manufacturing cell. The setup was designed with scalability in mind, allowing many cells to be run in parallel to meet production goals. The system performs three separate functions. It electrospins polymeric fiber laden with an active pharmaceutical ingredient (API) from an electrically charged spinneret to a grounded collector rod. Upon the completion of the spinning process, the rod is withdrawn into a pill die, where a stripper plate at the bottom of the die strips the pharmaceutical material from the rod. Finally, an upper punch descends into the die and the material is compressed into a final tablet geometry. Fig. 3-1 provides a an overview diagram detailing the steps in this process which will be explained in further detail in following sections.

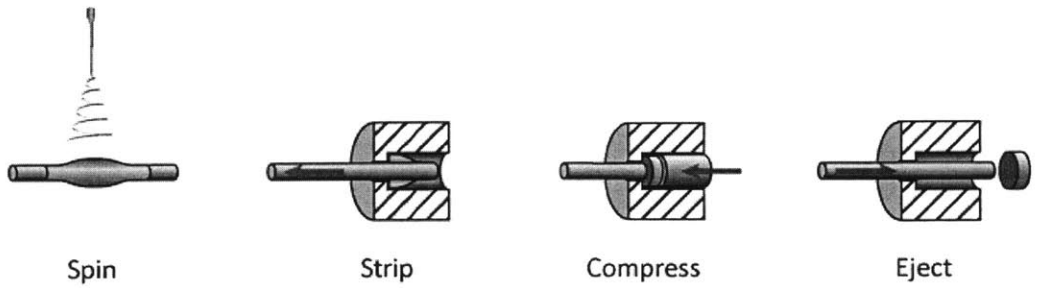

Figure 3-1: Overview of process components

The full experimental setup with final, rotating, horizontal collector rod configuration is displayed in Figure 3-2.

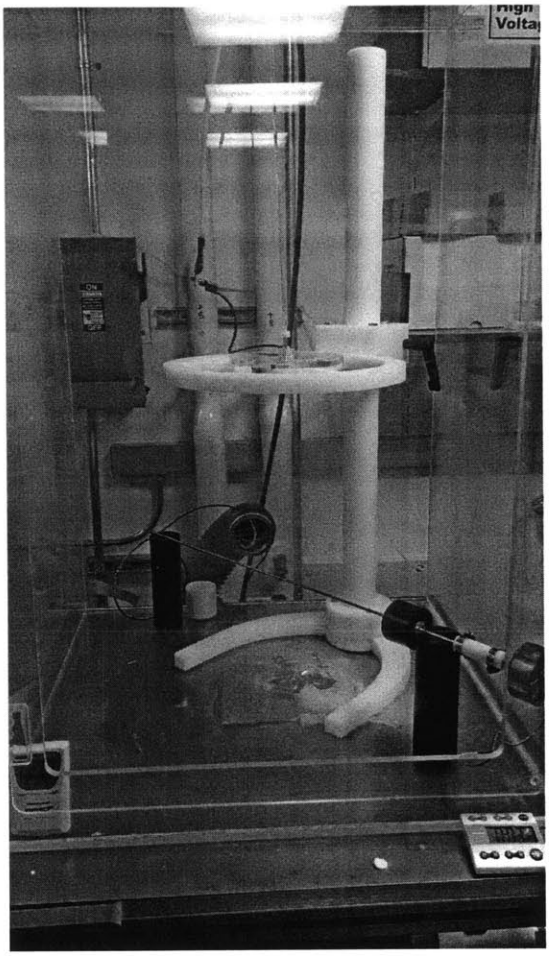

Figure 3-2: Full experimental setup in experiment enclosure

3.1 Power and Pumping

Electrospinning requires both a high voltage power supply and a source of pumping head. Electric potential was supplied by a 50 kV, 20 W benchtop power supply (Gamma High Voltage Research ES50P-20W/DDRM/PRG). The polymer solution was pumped via a syringe pump (Harvard Apparatus PHD2000 Infusion), through a length of tubing and finally through the system spinneret.

3.2 Spinneret

The spinneret in an electrospinning setup is an electrically conductive part that is charged to the applied spinning voltage, and from which the spinning solution forms jets. Initial research focused on new spinneret head designs as the primary driver of electrospinning process performance, and a series of increasingly detailed spinneret heads with various spinning nozzle geometries were designed, produced and tested. The design process, iterations and test results from these experiments can be found in Appendix A. However, the test results from these experiment trials found that these spinneret designs had little influence on fiber drying and collection, which was instead driven mainly by collector geometry. This seemed to result from the fact that the nozzle designs only affected the geometry and number of the fluid jets at their origin, while the electric fields generated by the collector geometry affected the fiber during its entire trajectory. All subsequent research focused on optimizing the embodiment of the collector, as it was found that collector design could enable a much higher degree of control over fiber deposition. Once the design focus shifted to the collector and die, electrospinning experiments were carried out with stainless steel blunt-end needles, with all final trials carried out specifically with 25 gauge needles, Figure 3-3, in order to constrain differences in electrospinning performance to changes in the collector design.

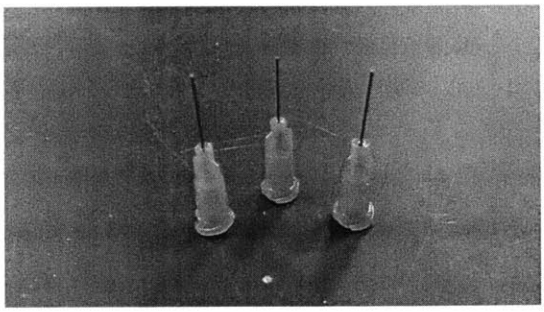

Figure 3-3: Stainless steel dispensing needle used in final experiments

3.3 Collector Development

The design of the collector underwent a series of iterations, beginning as an aluminum plate, continuing as an aluminum plug inside a pill die, to its final embodiment as a horizontal rod, described in Section 3.4. The successes and failures of each iteration drove the design of the next collector.

The first collector plate design was a 300 mm x 300 mm square aluminum plate. Experiments with the plate collector characterized the 'spot size' of the needle spinnerets, as detailed in Figure 3-4. The spot size is the maximum dimension of the circular distribution of fiber material desposited on the collector. Baseline spot size measurements were taken from simple electrospinning setups with a needle and the plate collector. Additional ancillary ring electrodes were added in later experiments on electrostatic lensing, in order to focus the applied electric fields and shrink the spot size. Efforts to shrink the spot size did reduce the characteristic diameter of the spot from around 180 mm to 30 mm, but a plate collector was not found to produce fiber deposition which could easily be transformed into common tablet geometries.

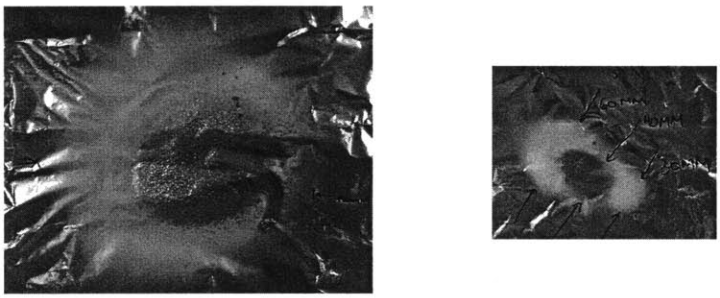

Figure 3-4: Spot size experiment, without ancillary electrodes, 180 mm diameter (left) and with best configuration, 30 mm diameter (right)

The goal of the second design was a collector that would promote easy tablet formation, and which utilized the electrostatic focusing electrodes from the collector plate setup. This iteration attempted to deposit the spun fibers directly into a pill die orifice, a setup which can be found in Figure 3-5.

The goal of this design was to produce electric fields which concentrated the fibers along the central axis of the setup by the time the fibers arrived at the die mouth,

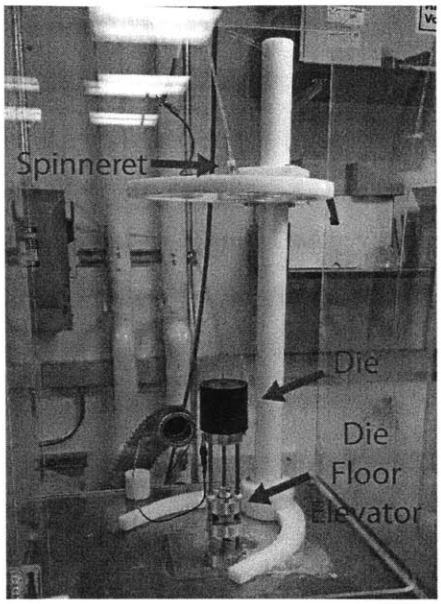

Figure 3-5: Direct-to-die electrospinning setup

and collect on an aluminum plug at the bottom of the die that formed the die floor. Experimental results demonstrated only a partial success at the stated goals of this collector design. While fibers were concentrated at the die orifice, they had a tendency to collect on the edge of the orifice, as seen in Figure 3-6, where there was a sharp edge and thus a slight electric field concentration. Fiber deposition inside the die itself was minimal.

Figure 3-6: Fiber deposition around die orifice at edge

It was unclear whether the strength of the electric field around the aluminum plug

collector was an issue in the direct-to-die system, so a die floor elevator was developed that could re-position the aluminum plug in the die cavity. This enabled the die floor to translate up and down with respect to the die. Experiments were run with the die floor located at the upper surface of the die cavity, as well as with the plug slowly descending into the die. This succeeded in producing a much tighter fiber deposition pattern on the aluminum plug, but both experiment runs resulted in laying down too much fiber outside of the collector plug, as displayed in Figure 3-7 to be successfully implemented as a commercial process.

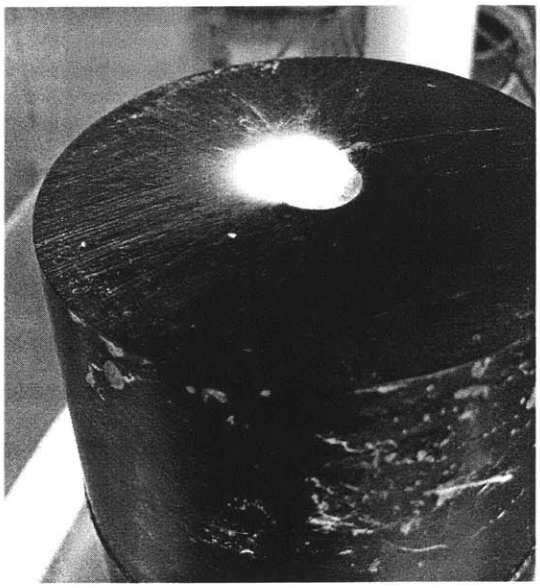

Figure 3-7: Fiber deposition on elevated die floor

At this point, inspiration was drawn from lightning rods, whose purpose is to provide the path of least electrical resistance in a volume of space. While the experiments in this research avoid the electrical breakdown and arcing found in lightning strikes, a similar collector design which provides a focal point for an electrostatically-driven process is desired. Thus a collector was developed in which a 50 mm long thin rod, smaller than the diameter of the 12 mm tableting die, projected out from the tableting die, with the ability to withdraw into the die during or after the spinning process. The rod was aligned axially with the electrospinning needle, and experimental trials found it lacked the ability to effectively collect electrospun fibers in a useful

manner. However, it was proposed to rotate this collector 90°, which resulted in the final horizontal rod collector design.

3.4 Horizontal Collector Rod

The collector used in the final setup, Figure 3-8, is a 3.76 mm (0.148 in. nominal) diameter rod, 600 mm long, which is mounted horizontally, perpendicular to the axial direction of the electrospinning needle.

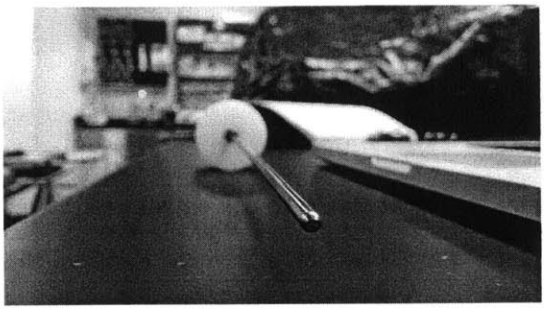

Figure 3-8: Horizontal collector rod

The rod is composed of a hard (Rockwell B89, see material properties section) multipurpose O1 tool steel, a design decision made to ensure that the stripping action of the rod passing through the stripper plate, described below, does not mar the surface of the collector and cause a reduced capability to strip. The most significant feature of the collector rod is its orientation perpendicular in relation to the spinneret. This configuration presents a 600 mm long surface on which to deposit fibers.

This collector configuration is cantilevered from the tableting die, and will suffer from some deflection due to self-weight. The loading situation can be accurately modeled as a cantilever beam with a uniformly-distributed load, as seen in Figure 3-9.

Theory from structural mechanics, Equation 3.1, describes the maximum tip deflection of the beam in this configuration:

$$\Delta_{max} = \frac{\omega l^4}{8EI} \tag{3.1}$$

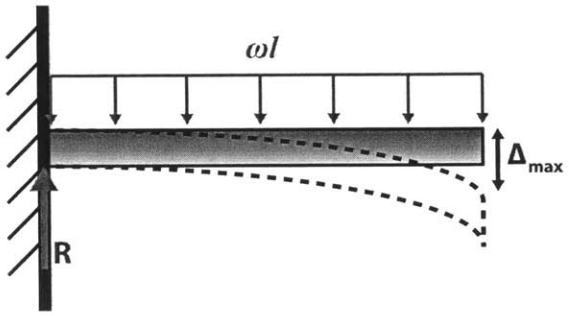

Figure 3-9: Cantilever beam with uniform load

Where Δ_{max} is the maximum deflection of the beam, ω is the beam weight per unit length, l is the beam length, E is the modulus of elasticity and I is the cross-sectional moment of inertia. Equation 3.2 is the moment of inertia, I for a beam of circular cross section:

$$I = \frac{\pi d^4}{64} \tag{3.2}$$

Where d is the rod diameter. At a rod diameter of 3.76 mm and length of 600 mm, the max deflection at the tip of an O1 tool steel collector rod is 0.75 mm, less than 0.25% of the distance between the spinneret and collector. This ensures that any deflection of the unsupported side of the collector rod is unlikely to cause any fiber distribution issues, since it results in a minuscule difference in spinneret-collector distance.

This collector embodiment has several advantages over current collector designs, such as conductive belts or flat metal plates, because it encourages fiber collection in a geometry that is well suited for simple and rapid post-spin transfer to a pill die. In comparison, the process of transferring a sheet of electrospun mat material collected

on a planar surface to a cylindrical die cavity is non-trivial and may require many intermediate folding steps.

3.5 Stripper Plate and Die Design

The tableting die component of this system contains features designed to smoothly strip fiber material from the collector rod and then compress it into the final pill geometry. The die used in final experimental trials had an inner cavity diameter of 12 mm. The floor of the die consists of a metal plate with a hole in the center, whose diameter creates a precision slip fit with the collector rod. The shape of this plate forms a negative of the desired geometry of the bottom half of the final tablet. A cut-away cross section of an example die, detailing the stripper plate feature and bearing surfaces can be seen in Figure 3-10.

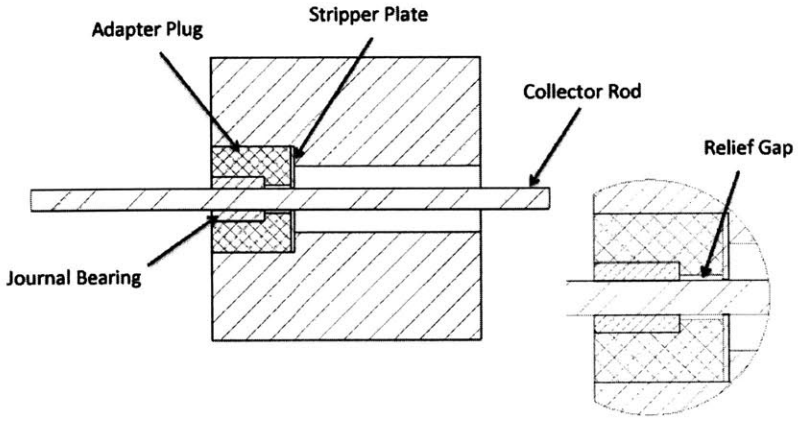

Figure 3-10: Cut-away view of stripper plate and bearing surfaces

The design of the bearing surfaces seen in Figure 3-10 is notable because of the spacing between the stripper plate and journal bearing. The two bearing surfaces are designed according to Saint-Venant's Principle, which suggests a ratio of 1.6:1 or greater for the spacing of linear bearings to the diameter of the shaft, to minimize bearing lock-up and premature failure due to offset loading. In the final design presented here, the minimum spacing between the two bearing surfaces is 9.65 mm,

compared with a collector rod diameter of 3.76 mm, for a ratio of 2.5:1, well above the 1.6:1 minimum acceptable ratio suggested by Saint-Venant.

The rim of the central hole in the stripper plate is ground to a sharp edge in order to effectively strip the fiber from the collector rod. Due to the desired domed or cylindrical pill geometries produced via this system, the stripper edge will always form a rake angle of $\leq 0°$ with the collector rod, as seen in Fig. 3-11.

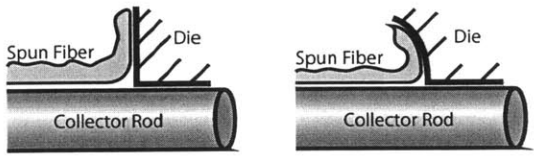

Figure 3-11: Minimum (left), and example negative die floor rake angle (right)

A negative rake angle is less ideal than a positive rake angle in this scenario, since the force produced normal to the cutting surface tends to compress the fiber material against the collector rod, rather than lifting it off of the rod as in the case of a positive rake angle, see Figure 3-12.

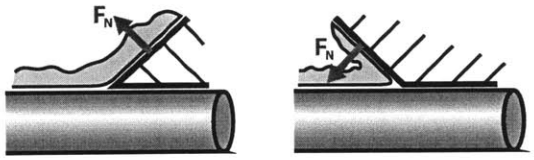

Figure 3-12: Normal force due to a positive (left) and negative rake angle (right)

Since the geometries of standard tablet shapes require the cutting edge to form a non-ideal neutral or negative rake angle, a sharp edge is important to ensure that the stripper plate overcomes the adhesive force attaching the fibers to the rod, rather than shearing the fibers themselves and allowing a skin of fibers to pass beneath the floor of the die. Fig. 3-13 demonstrates an example of acceptable sharp edge and an example of unacceptable worn edge geometry.

A 316 stainless steel washer served as the stripper plate for prototyping purposes, in order to quickly replace defective or failed plates, but stripper plate was designed to be made from a case-hardened stainless steel in production models for increased

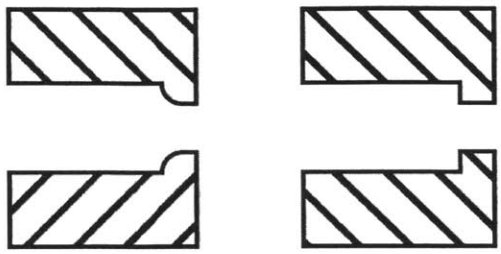

Figure 3-13: Undesirable (left) and effective (right) stripper plate geometry

wear resistance.

3.6 Collector Rod Rotation

Electrospinning process tests with a static, horizontal collector rod demonstrated that while the the horizontal rod entraps nearly all fibers spun during the process, it does so with unequal distribution about the circumference of the rod. This in turn had a tendency to produce inhomogeneous pills with uneven mechanical properties across the width of the pill, since the fiber material was unevenly distributed in the die after the stripping process. To solve this problem, a DC motor was attached to the collector rod via an insulating Delrin shaft connector, as seen in Figure 3-14.

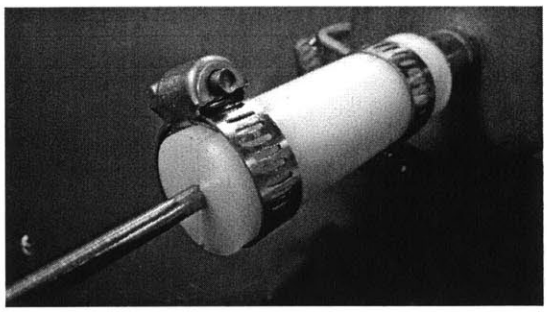

Figure 3-14: Delrin shaft connector detail

The collector rod could no longer be grounded by an alligator clip since it was rotating, so a conductive sliding contact was attached to the end of the collector rod, as seen in Figure 3-15. This allowed the collector to main electrical contact with ground while rotating.

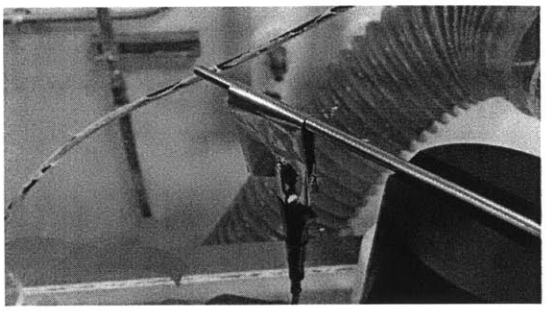

Figure 3-15: Sliding ground contact

3.7 Upper Punch and Compression

A tableting press (Gamlen Tableting GPT1) was adapted to provide the compression force for the prototype system. Pill dies were designed to interface with the press and a 12 mm diameter die was built to perform with a corresponding punch. The tableting press provided a simple measurement of compaction force as a function of position of the punch. The punch compressed the fiber material until the onboard load cell detected that the desired load limit had been achieved. The compaction process is detailed in Figure 3-16.

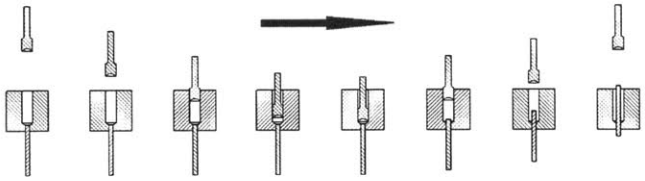

Figure 3-16: Post-process compaction intermediate steps for a single pill compaction

3.8 Die Plugs

Since the collector rod could not fit in the tableting press used in the compression experiments, a small plug was created to form the die floor for the tableting dies during compression. The plug replaced the functionality of a withdrawn collector rod that would be present in a scaled-up version of the setup. The die plug can be seen in Figure 3-17.

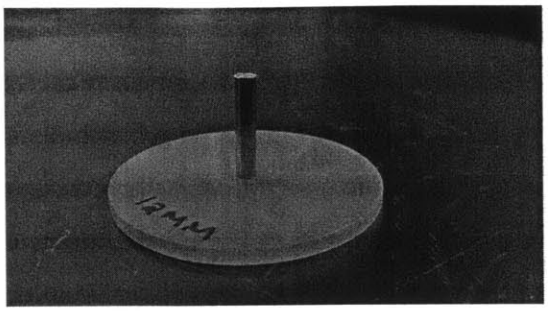

Figure 3-17: Die plug detail

3.9 Non-Conductive Stand

The experimental setup is designed such that the electric fields that drive the electrospinning process are as close to axisymmetric around the spinning needle as can be reasonably achieved. As such, the stand used to suspend the needle must be non-conductive to avoid creating a secondary induced electrostatic field. The stand design is detailed in Figure 3-18. The stand includes a vertical scale to determine the spinneret to collector (SC) distance as well an adjustable clamp to vary the SC parameter. A cantilevered arm design was used to hold the spinneret receiver to facilitate frequent SC adjustment via the single compression clamp. A gantry-style design was first considered but was rejected in favor of the cantilever design due to the decreased adjustment time and effort required to change the SC distance with the cantilever-style stand.

3.10 Material Selection

3.10.1 Delrin©

Delrin©has excellent electrically insulating properties and is both highly machinable and structurally rigid. It was an attractive material choice for the experimental stand, as it minimized distortion of the electric fields generated in experiments.

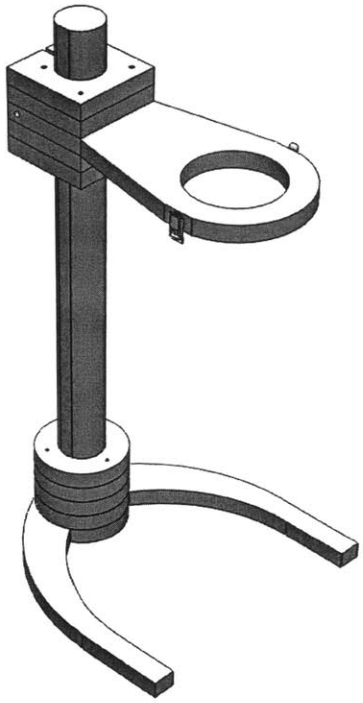

Figure 3-18: Non-conductive stand detail

3.10.2 Aluminum Alloy 6061-T6511

Aluminum 6061-T6511 was chosen as the metal for prototype development for its mechanical properties. Aluminum alloy 6061 exhibits excellent machinability. The T6511 temper includes a solution heat treatment, artificial aging, and internal stress-relief treatment performed by stretching [6]. This temper ensures that the alloy will undergo minimal physical change due to internal forces and reactions of surface chemistry post-machining, producing parts that meet the design tolerances. Aluminum 6061-T6511's properties are:

- Hardness: Rockwell B60
- Yield Strength: 276 MPa
- Modulus of Elasticity: 68.9 GPa

- Density: 2700 kg/m^3

3.10.3 316 Stainless Steel

- Hardness: Rockwell B79
- Yield Strength: 290 MPa
- Modulus of Elasticity: 193 GPa
- Density: 8000 kg/m^3

3.10.4 O1 Tool Steel

- Hardness: Rockwell B89
- Yield Strength: 345 MPa
- Modulus of Elasticity: 190 GPa
- Density: 7800 kg/m^3

THIS PAGE INTENTIONALLY LEFT BLANK

Chapter 4

Experimental Methods

Experiments were run on the test setup in an attempt to test a full range of configurations of collector designs. Experiment design was guided by a desire to replicate pharmaceutical-grade manufacturing conditions and system requirements as early in development as possible, rather than attempting to re-design lab-driven processes for use in industry *ex-post facto*. Basic electrospinning performance with the system was characterized by developing two graphs relating spinneret-collector (SC) distance and solution flow rate to the system critical spinning voltage at which jet initiation began. The process was further developed by identifying ideal spinning parameters which reliably produced replicable spinning results. These parameters were then applied to the final rotating collector rod concept. The goal of the experiments was to enable future scaling of the electrospinning process and physical system to full industrial scale production.

The basic experimental design involved electrospinning a solution of polyvinylpyrrolidone (PVP) and ethanol to various collector embodiments. A solution of 8 wt% 1.3 MDa PVP (Sigma Aldrich) and ethanol was used in all final experimental trials. After the formulation was prepared, a syringe was filled with solution, and flexible polyurethane tubing was connected between a luer-lock barbed fitting attached to the end of the syringe and a similar fitting attached to the back of a blunt-end needle or other spinneret design. Any air in the syringe was expelled, and solution was manually propelled into the tubing. The syringe was then loaded into the syringe pump.

The experimental setup was checked to ensure that the spinneret was attached to the high voltage power supply and that the collector was grounded. The pump was run until dripping was observed from the needle tip and then the power supply was turned on and a specified voltage was applied to the spinneret. Electrospinning proceeded for a specified length of time until a desired volume of material had been spun and then power was shut off to the system. The full experiment procedure followed in final experiments can be seen in Figure 4-1.

Step #	Step
1	Stir solution for >5 min
2	Record temperature and RH
3	Select die and collector rod, place in enclosure, record selections
4	Set spinneret-collector (SC) distance and record
5	Cut tubing to length, add fittings
6	Fill syringe w/40-50mL of solution
7	Extrude solution to w/in 10 cm of nozzle
8	Fixture syringe in pump
9	Attach nozzle to fluid line
10	Check ventilation operation
11	Remove any unnecessary equipment from enclosure and shut door
12	Set syringe pump syringe diameter and flow rate
13	Set timer according to formulation and flowrate chart at right
14	Start syringe pump
15	Set voltage to desired level after solution enters needle
16	Start timer when spinning begins
17	Monitor process for dripping
18	When timer stops, shut off power supply and stop syringe pump

Figure 4-1: Experimental procedure checklist

4.1 Solution Preparation

The spinning solution was prepared in advance of experimental trials as close to the actual experiment run as possible, in order to minimize solution aging. Since the ethanol solvent is volatile at room temperature and can quickly evaporate, care was taken to prevent this and maintain constant solution properties. The formulations used in experimental trials were specified by the weight percent of each of constituent ingredients. To produce the actual solution, dry solid constituents were first individ-

ually weighed and then added to a dry clean flask. The flask was placed on a scale (Ohaus SP202 AM), which was then tared, and the liquid solvent was added until the prescribed solvent mass was achieved. A magnetic stir bar was added to the flask, and the solution was mixed on a stir plate (VWR 7x7 CER Hotplate/Stirrer) for at least 15 minutes. Stirring times were extended for solutions containing higher percentages of solute. Higher-viscosity solutions which retained small air bubbles after stirring were subjected to a degassing procedure in an ultrasonic water bath (Bransonic Ultrasonic Cleaner 8510R-MT). A spreadsheet was developed to automatically calculate solution recipes based on weight percent and volume desired. An example recipe generated from this spreadsheet can be found in Table 4.1.

Solution by Polymer Mass	
Concentration (wt%)	8.00%
Polymer	1.3 MDa PVP
Mass Dry Polymer (g)	5.00
Polymer Molecular Weight (g/mol)	1,300,000
Solvent	Ethanol
Mass Solvent (g)	57.5
Solvent Density (g/mL)	0.789
Volume Solvent (mL)	72.88
Solution Recipe	
Mass Dry Polymer (g)	5
Volume Solvent (mL)	72.88

Solution by Solvent Volume	
Concentration (wt%)	8.00%
Polymer	1.3 MDa PVP
Mass Dry Polymer (g)	13.72
Polymer Molecular Weight (g/mol)	1,300,000
Solvent	Ethanol
Mass Solvent (g)	157.8
Solvent Density (g/mL)	0.789
Volume Solvent (mL)	200.00
Solution Recipe	
Mass Dry Polymer (g)	13.72
Volume Solvent (mL)	200.00

Enter Value
Calculated Value

Table 4.1: Example solution recipe

4.2 Critical Spinning Voltage Experiments

All documented observations of the electrospinning process find that above a certain, critical voltage, effluent solution from a downward-facing spinneret stops dripping and instead produces a thin liquid jetting phenomena first described by Taylor [9]. This jetting occurs when electrostatic forces overcome surface tension effects. In order to develop a range of parameter values for later testing of electrospinning performance, it was desired to know the critical spinning voltage of the experiment setup. Theory points to the critical voltage as a function of spinneret-collector (SC) gap distance, since Coulomb's Law maintains that the electrostatic force between two charges is proportional to $1/r^2$, where r is the gap distance. Thus decreasing the gap distance should also decrease the critical spinning voltage above which spinning begins.

Initial electrospinning trials at various voltages and SC gap distances had identified an SC gap distance of 300 mm as an distance which produced dry fibers at an applied voltage of 30 kV, while still allowing higher voltages to be tested by the 50 kV experimental power supply. Utilizing these values as starting points, two sets of experiments were run. The first tested the theory that critical spinning voltage increased with gap distance. Electrospinning trials were run at a range of SC gap distances from 150 mm to 300 mm, with an experimental solution flow rate of 0.5 mL/min. The applied voltage at which a stable Taylor cone was established was recorded for each gap distance. The collector rod was cleaned of deposited fibers and liquid solution between runs, in order to eliminate any electrically insulating effects these might have on the system. The second set of trials focused on the identified 300 mm gap distance and tested whether the system solution flow rate had any influence on the critical spinning voltage. The SC gap for these experiments was held at 300 mm and the critical electrospinning voltage was recorded for flow rates of 0.5, 1.0, and 1.5 mL/min.

4.3 Horizontal Static Rod Characterization

A two factorial experiment design was run to empirically determine sets of stable system operating parameters for a horizontal static rod (HSR) collector. The physical setup for these experiments was very similar to the final proof-of-concept design and can be found in Figure 4-2.

The two tested parameters were the applied electrode voltage and the system solution flow rate. The collector rod was kept static during the experiments to ensure that electrospinning results for the setup were solely a function of the particular voltage and flow rate values tested. Trials were run at flow rates of 0.5, 1.0 and 1.5 mL/min and applied voltages of 30, 40 and 50 kV.

Experiments were designed to produce a 0.2 g tablet for all experimental trials, which was identified as a common tablet size. Run times were calculated based on the flow rate used and are detailed in Table 4.2.

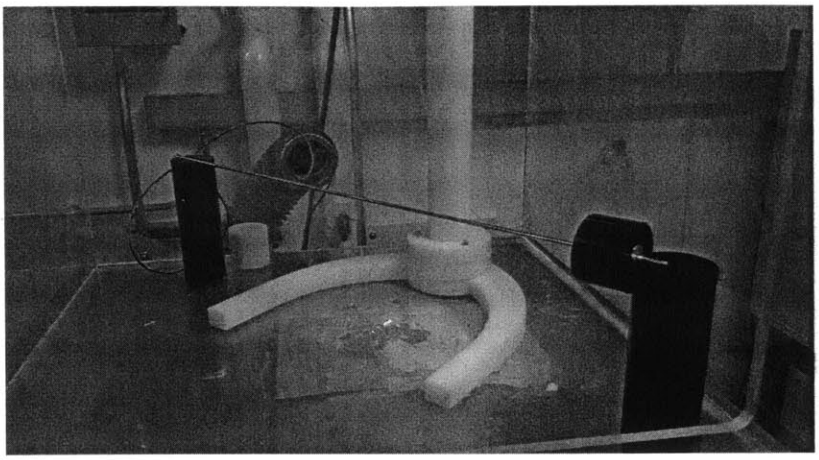

Figure 4-2: Horizontal static collector rod setup

Timer Chart	0.2 g pill	
Formulation	8 wt% 1.3 MDa PVP + ETOH	
Flowrate (mL/min)	Timer (min)	Timer display
0.5	5.00	5:00
1	2.50	3:00
0.75	3.33	3:20
1.5	1.67	1:40

Table 4.2: Experiment run times by flow rate

4.4 Rotating Collector Rod Trials

Using the optimum parameters determined from the HSR collector experiments for a flow rate of 0.5 mL/min, system performance was then tested while the collector rod was rotated at approximately 300 RPM. The experimental procedure was exactly the same as for the HSR trials, with the exception that collector rotation was initiated before solution was pumped through the system. The finished spinning results were compared to results of HSR experiments using the same parameters but with a static collector.

4.5 Multiple Needle Rotating Collector Rod

A final electrospinning experiment was performed to test whether multiple needles could be used in the setup to increase the bulk flow rate of the system, since exper-

imental evidence suggested that a single needle of any given diameter has an upper bound on the flow rate it can successfully electrospin. Thus, to push the bulk flow rate past this point, multiple jets are required. Two needles were used in the experiment, spaced 200 mm from each other, and each attached to the fluid loop with the same length of tubing to eliminate pressure head differences. The multi-needle experiments attempted to electrospin at two different SC distances, 300 mm and 250 mm and at 40 kV and 20 kV applied voltage respectively. The collector was again rotated at 300 RPM.

4.6 Stripping Procedure

If the electrospinning process in any horizontal collector rod experiment was successful, and no liquid solution was observed on the collector, the rod was manually pulled through a 12 mm diameter tableting die. Stripping was only performed if the deposited material consisted of properly spun fibers. It was found that material that had been deposited as a liquid, and subsequently dried, adhered to the collector rod and tended to jam in the clearance gap between the stripper plate and the rod. The stripped material tended to maintain its integrity as a continuous mat post-strip and, as can be seen in Figure 4-3, formed a compressed tube-like structure which often projected out past the die orifice.

The collector rod was also examined visually post-strip to ensure that a reliable, clean strip had occurred. This observation was important in conjunction with the observed quality of the spun fibers, as it allowed characteristics of different spinning qualities to be correlated with strip quality.

4.7 Tablet Compression

At the conclusion of the stripping procedure, the test die was filled with the fiber tube shedded from the collector. A die plug was manually inserted into the bottom of the tableting die to form a uniform flat die floor. The entire die assembly was then placed

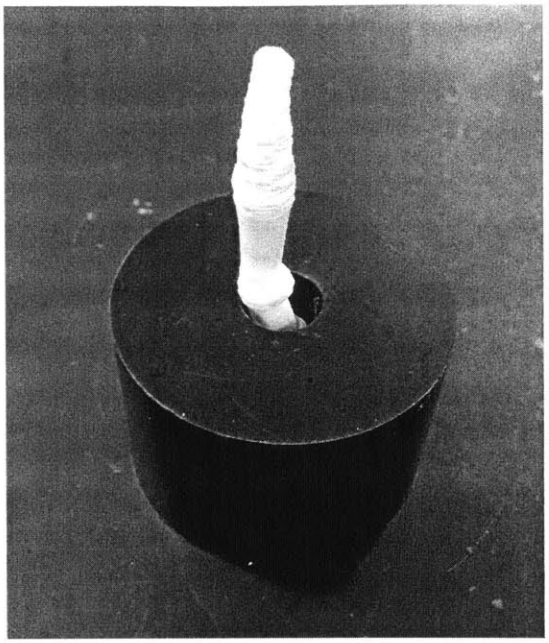

Figure 4-3: Post-strip fiber 'tube' in die

into the tableting die, and a compression trial run. The tableting die was equipped with a 500 kg load cell and set in all experiments to perform continual compression on the material in the die until a load measurement of 400 kg was reached. Due to the measurement lag, this generally resulted in a maximum compression force of around 420 kg. A peak load hold, or dwell operation was desired, but it was not a function of the tableting press used in these experiments and is left to future work. The tableting press and die can be found in Figure 4-4.

Once the upper punch automatically rose out of the die post-peak load, the finished tablet could be ejected and its mass measured.

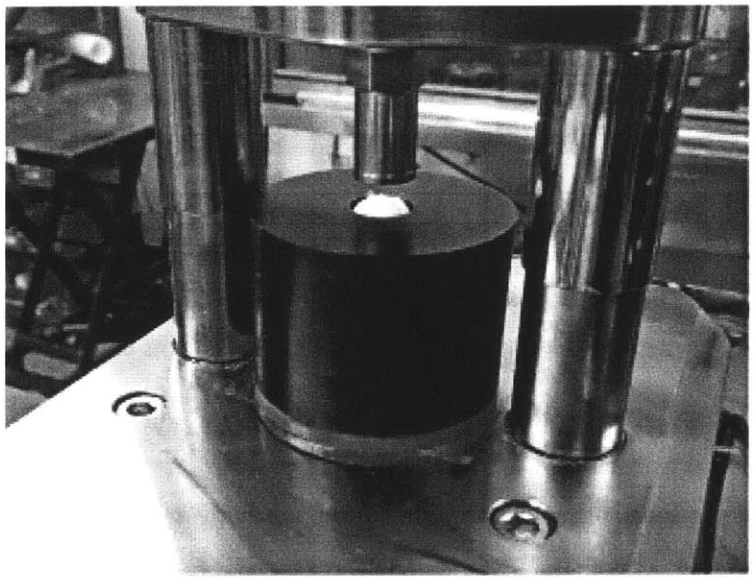

Figure 4-4: Tableting press and die, die plug inserted

Chapter 5

Results

The results of the experiments which characterized and tested the horizontal collector rod setups are presented in this chapter. Additional work on the performance of various spinneret geometries developed early in the research process are detailed in Appendix A, but are not shown here, because the observed results did not directly affect or influence the performance of the horizontal collector rod system.

5.1 Critical Spinning Voltage

Experiments were run to characterize the critical spinning voltage of the process, above which jetting will occur from the spinneret. This was tested with the same physical setups as later horizontal rod spinning experiments. The critical spinning voltage characterizations were performed to test whether variations in the solution flow rate or system spinneret-collector (SC) gap distance were fundamentally changing the voltage required to initiate jetting from the spinneret. The electrostatic force between two charges is described by Coulomb's Law, whose general form is Eq. 5.1:

$$F \propto \frac{q_1 q_2}{r^2} \tag{5.1}$$

Where F is the electrostatic force between the charges, q_1 and q_2 are the charge magnitudes in coulombs, and r is the distance between the charges. For any set of

constant charges, the electrostatic force is simply proportional to the inverse square of the distance between them. A simple experiment was run to confirm this relationship, testing the effect of the distance between the spinneret and collector on the critical applied voltage required to induce spinning. At each SC distance tested, solution was pumped through the system at a constant flow rate of 0.5 mL/min, while the voltage applied to the spinneret was increased until visually stable jetting occurred. The results are displayed in Fig. 5-1. The applied voltage required to produce the same electrostatic force increases proportionally to r^2 as the spinneret-collector (SC) gap distance is increased. The data supports a $1/r^2$ relation between electrostatic force and SC distance.

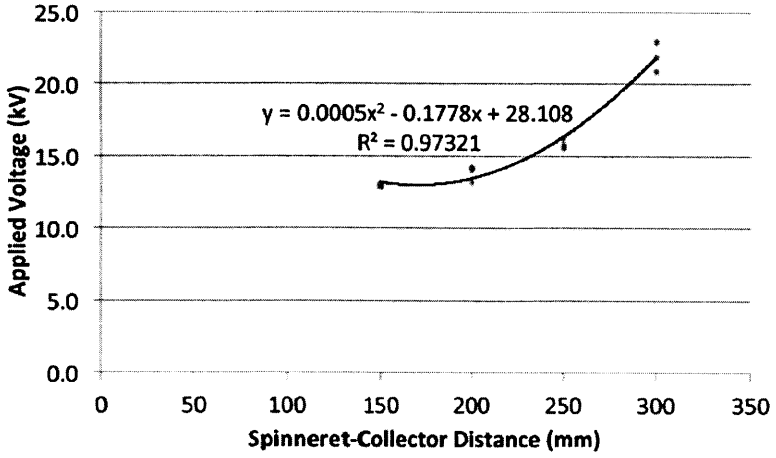

Figure 5-1: Critical spinning voltage versus spinneret collector distance

Since Coulomb's Law does not account for surface tension and gravity, the effect of flow rate variation on the critical spinning voltage was also tested. For a range of flow rates from 0.5 to 1.5 mL/min, the applied voltage was again increased until jetting occurred, at a constant SC distance and flow rate. The results of this experiment are documented in Fig. 5-2.

As can be observed in Fig. 5-2, there was little significant difference in the critical spinning voltage over the range of flow rates utilized in this research.

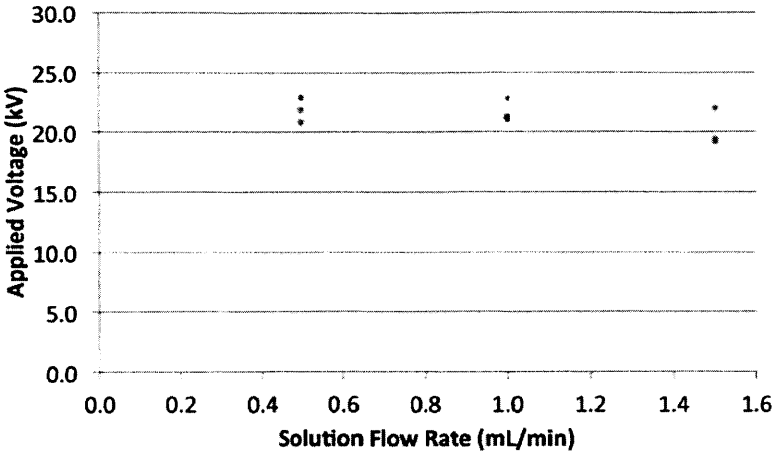

Figure 5-2: Critical spinning voltage versus solution flow rate

5.2 Horizontal Static Rod Experiments

The horizontal static rod (HSR) experiments tested the spinning performance of a range of experimental flow rates ranging from 0.5 mL/min to 1.5 mL/min and applied voltages of 30 kV to 50 kV, all with a SC distance of 300 mm. This produced a performance chart seen in Figure 5-3 which details the success or failure of electrospinning at the given parameters.

These results found that for a SC distance of 300 mm there was a unique parameter combination of 0.5 mL/min flow rate and 40 kV applied voltage which was capable of spinning the desired pill mass.

5.3 HSR and Rotating Rod Comparison

The experimental results of electrospinning at the successful HSR flow rate of 0.5 mL/min, applied voltage of 40 kV and SC distance of 300 mm were then compared to experimental results using a setup with the same parameters, with the addition rotating the collector rod at 300 RPM. The results of the rotating rod experiments show a vast improvement in circumferential uniformity of the fiber distribution as compared with the HSR results, as detailed in Figure 5-4. This uniformity appears

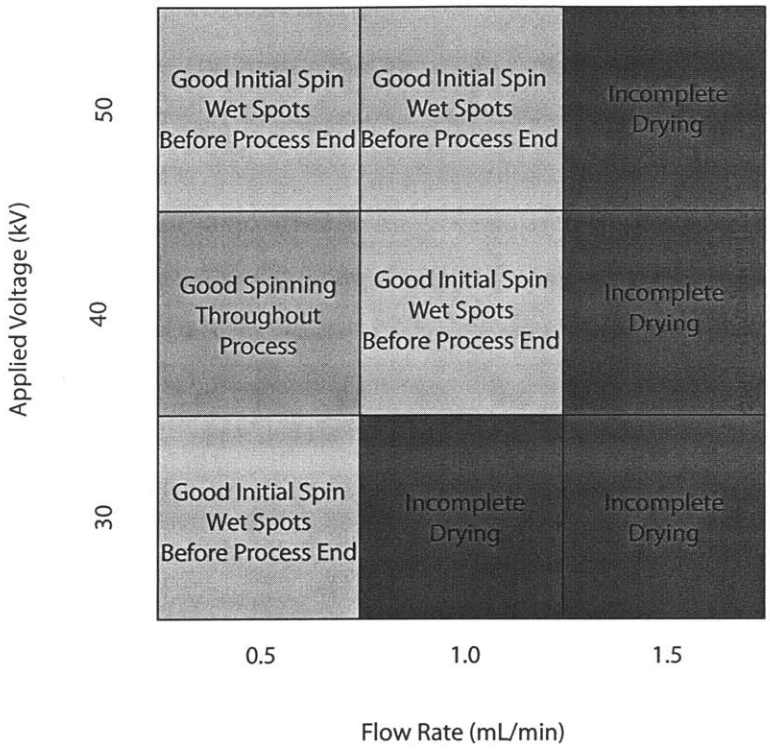

Figure 5-3: HSR electrospinning performance at various spinning parameters

to result from two phenomena: first, the rotation causes all of the rod surface area to see equal time facing the spinning needle, and second, any long fiber sections which tended to drape over the collector rod in the HSR experiments were rolled up onto the rod in a manner similar to a retracting winch. The two combined factors contributed to the more compact and uniform distribution seen in Figure 5-4 for the rotating rod as compared to the HSR results.

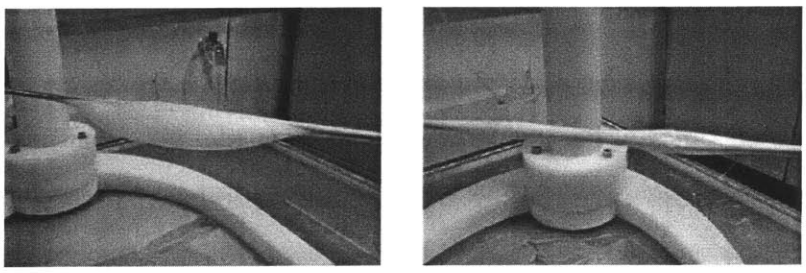

Figure 5-4: 0.2 g spinning run by HSR (left) and rotating collector rod (right)

5.4 Compression Results

The compression process yielded results which signaled a non-uniform radial distribution of material in the die. Compression results from the HSR collector also demonstrated that in the HSR trials, there was a non-uniform circumferential distribution of material as well, which was expected since the collector did not see a uniform distribution of deposited fiber material around its long axis. Compression data from the tablet press was very similar across all compression trials, and an example plot from one of the HSR experiments is found in Figure 5-5.

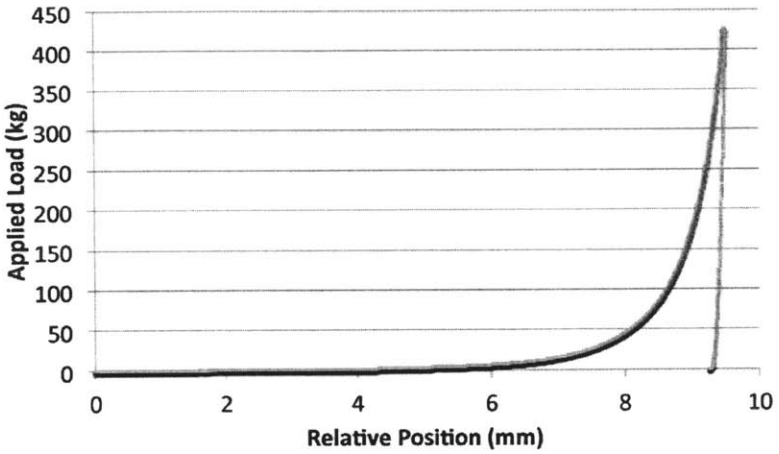

Figure 5-5: Example compression force versus punch distance profile

The load cell measured average force across the tablet being produced, but visually, it was clear that higher compaction pressures built up near the center of the die floor, while near the die walls less force was transferred. An example of this showing a ragged, less-compressed tablet edge is demonstrated in Figure 5-6.

This problem would likely have been solved by an increase in material volume in the die. The final 0.2 g tablets had an average thickness of 1.9 mm, which resulted in a thickness to diameter ratio of just under 1:6. The fiber material did not seem to flow sufficiently under compressive pressure to fill the die to its edges - rather, the material appeared to remain mostly locally stationary, with larger compressive pressures building up in areas of greater fiber distribution around the center of the die

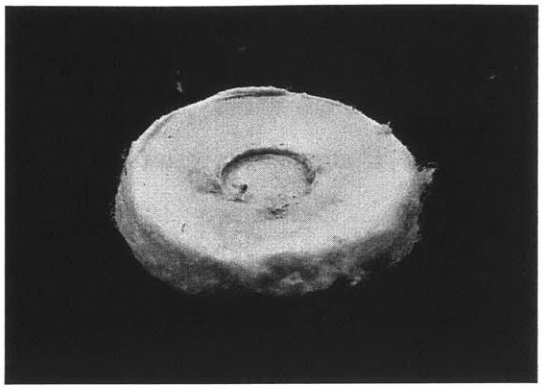

Figure 5-6: Variation in degree of compression across tablet surface, note frayed edge

floor. A larger volume of material in the die would allow more material to redistribute itself earlier on in the compression process, resulting in a more homogeneous tablet.

The compression process did appear to be robust and repeatable as demonstrated in Figure 5-7, in which nearly identical tablets were produced from a variety of different flow rates and spinning voltages.

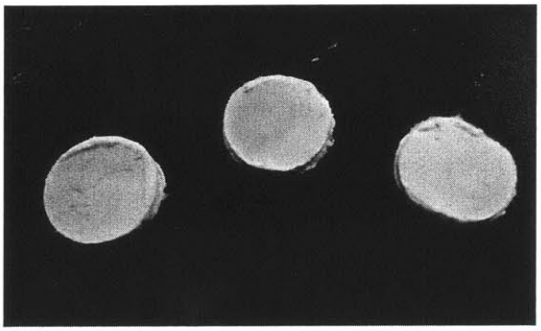

Figure 5-7: Compressed tablets produced with varying spinning parameters

Chapter 6

Conclusion

A manufacturing process and proof-of-concept system were developed to continuously manufacture pharmaceutical tablets. The physical device electrospins thin polymer fibers downwards from a spinneret needle to a grounded horizontal, rotating collector rod. Post-spinning, the rod is withdrawn through the bottom of a tableting die, and the deposited fiber material is removed from the rod by a stripper plate in the bottom of the die. A die punch subsequently descends into the die cavity, where it compresses the polymer fiber material into a solid, monolithic tablet. Finally, the collector rod ascends back out of the die and ejects the compressed tablet.

The proof-of-concept system demonstrated the feasibility of continuous manufacturing equipment that could meet the functional requirements identified early on in the research. The horizontal rod collects all fibers created by the spinneret, minimizing the presence of airborne API particulates which are created by current powder-based systems. The system has the capability to accept a liquid polymer and API input and produce solid tablets from this solution. Additionally, the process can continuously electrospin fibers, and with a constant supply of solution, an industrial-scale version could continuously exchange fully-loaded collector rods for clean ones quickly and efficiently, maintaining the continuity of the spinning process. It was demonstrated that scale-up to Novartis' production goals was possible. While the system demonstrated in this research did not have the capability to meet the required flow rates, other preexisting spinneret technologies do have the required flow capacity in

order to meet these goals. Experimental trials proved that the electrospinning process is reliable and repeatable, producing consistent electrospinning results across a range of trials when the process parameters were held constant. Once the process is optimized for the particular physical setup geometry, electrospun fiber deposition produces stable results.

The tableting process developed here also has distinct advantages for use in an industrial manufacturing facility. It has few moving parts, and can produce tablets with only three linear motions, which is important for system reliability and maintenance. The electrospinning process also minimizes solution drying time, as it produces resultant fibers with high surface to volume ratios, and does not suffer from a drying bottleneck. The entire manufacturing process is built from technologies which have seen proven success in other areas, and have been adapted for use in this research.

An electrospinning-based system for direct formation of tablets is a unique solution to the pharmaceutical industry's desire to move towards leaner, more agile manufacturing of future treatments.

Chapter 7

Future Work

The work in this research demonstrated a proof-of-concept system for continuous manufacturing of pharmaceuticals. It is left to future work to fully optimize the process in order to scale it for industrial production. There are a number of process improvements presented here that would enable the higher degree of process control necessary to meet the strict regulatory specifications which exist in the pharmaceutical manufacturing industry.

7.1 Continuous Process Monitoring by Machine Vision

One of the largest obstacles to a stable spinning process was a lack of a distinct, easily measurable metrics by which to electronically monitor and control the electrospinning process. Instead, in early experiments, the power supply voltage was adjusted manually in response to visually observed changes in and characteristics of the Taylor cone, or cones, developed in the experiment. As the spinning progressed, previously spun fibers appeared to incrementally insulate the grounded collector rod and it was necessary to increase the voltage in order to preserve the stability of the Taylor cone and the process. Later experiments chose an applied voltage high enough that the insulating effect did not have time to significantly affect the spinning process before the

desired amount of material had been deposited. Visually, this effect could be observed as the Taylor cone expanded length-wise and grew in diameter over time. The successful implementation of closed-loop feedback control driven by optical monitoring via machine vision is left to future work.

7.2 Stripping Movements

The stripping process used in the experiments in this research was a straightforward withdrawal of the collector rod through the bottom of the tableting die. While this method produced acceptable stripping, it was observed that rotating the collector rod during withdrawal tended to pack the fiber material into the die cavity in a more compact, helical geometry. This caused a tighter pre-compression packing of the spun material in the die, causing less fiber material to project out of the die. It is suggested that future research examine various stripping withdrawal paths, as tighter pre-compression packing of the spun fiber material may result in shorter required die cavities which still fully contain any deposited process material. Withdrawal paths which follow spiral curves, zigzag trajectories or even paths which resemble a peck drill machining operation should be considered.

7.3 Continuous Weight Monitoring

In addition to machine vision for continuous process quality monitoring, the addition of a load cell inside or underneath tableting dies would allow for continuous weight monitoring of the spun material on the collector rod. This in turn would enable real-time monitoring of the pharmaceutical deposition process and ensuring that tablets produced in the process fall within regulatory tolerance limits on the tablet contents. A load cell with a high resolution would also be able to monitor the process for out of control spinning, as the mass accumulation rate on the collector rod would be higher than expected in the event of incomplete fiber drying before deposition on the collector.

7.4 Solution Optimization for Improved Stripping Process

The equipment developed in this research was designed to utilize a polymer formulation that was found to readily produce consistent and well-formed fibers. However, in order to optimize the equipment and process developed, work should be performed on optimizing drug formulation. In particular, a formula which produces fibers with a high degree of self-adhesion, but with low attraction towards the metal utilized for the collector rod, would be well-suited for this system. Incomplete stripping of the spun fiber material from the collector rod is the biggest source of potential system waste and equipment malfunction A formulation with the aforementioned properties will decrease the likelihood of an incomplete strip.

7.5 Compression Characterization

The results from the compression trials demonstrated that compression of the fiber material into a pill geometry was both possible and reliable. However, the pills produced showed signs of non-homogeneous macroscopic tablet properties, which may have an effect on dissolution characteristics. A study should be performed on the density variation observed with respect to radial position on the tablet. Since it is desired for the tablets to have consistent properties across the body of the tablet, characterization work should be performed to optimize and identify the compression process that produces such tablets. The effects of different compression speeds, forces and peak load hold times should be investigated to determine optimum compression parameters.

THIS PAGE INTENTIONALLY LEFT BLANK

Appendix A

Spinneret Design

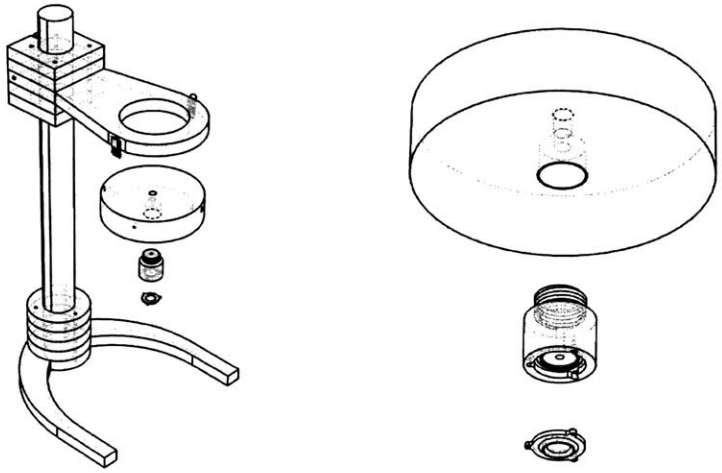

(a) (b)

Figure A-1: Exploded views of the quick swap nozzle experimental setup

A.1 Data Collection and System Monitoring and Control

Data collection and system monitoring and control subsequent to initial one-off experiments was performed with a National Instruments cDAQ-9174 modular data acquisition system chassis coupled with three data collection modules. The three modules

were an NI 9211 4-Channel, 14 S/s, 24-Bit, 80 mV Thermocouple Input Module; an NI 9208 16-Channel Current Input Module; and a NI 9401 8 Ch, 5 V/TTL High-Speed Bidirectional Digital I/O Module. Data was collected from an ambient thermocouple and a pressure transducer directly upstream of the nozzle. The NI cDAQ system also monitored and controlled different aspects of the experimental setup, such as controlling the die floor elevator and monitoring its two limit switches for system over-travel. Additionally, the high voltage power supply output voltage and syringe pump flowrate were controlled and enabled by NI cDAQ output.

A.2 Spinneret Receiver v1.0

The spinneret receiver, Figure A-2 is a 150mm diameter aluminum disk which the various spinneret heads can be attached to via a threaded hole in the receiver. The large diameter of the receiver in comparison to those of the various head designs ($\sim 25-35$mm) was a calculated design decision as it greatly simplifies the mathematical modeling of the system. The cantilever arm of the non-conductive experimental stand has two latches which connect to two mating clips on the receiver, allowing quick disconnection for ethanol cleaning and sonication of the entire receiver and head unit between experiments

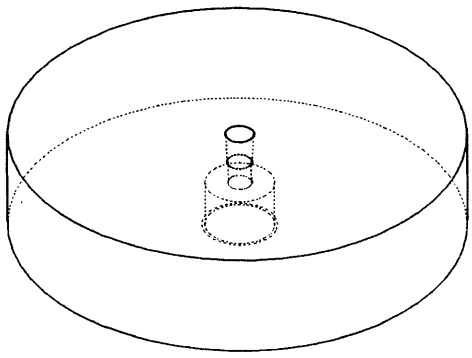

Figure A-2: Spinneret receiver detail

A.3 Integrated Spinneret Head

The integrated spinneret head in Figure A-3 attaches to the receiver through a UNF 1-12 straight threaded connection. The integrated spinneret head was the earliest produced spinneret design and featured an aluminum unibody design that incorporated the actual spinneret with the head. The spinneret itself was four milled slots tracing out the quadrants of a circle. Without any defining nozzle characteristics, however, the entire bottom flat plane of the spinneret head was wetted upon solution emission from the slots and jet formation had little correlation with the physical geometry of the spinneret.

Figure A-3: Integrated spinneret head detail

A.4 Quick-Swap Head

Initial results from the integrated spinneret head required a redesign in spinneret geometry, but due to the extended manufacturing time required to iterate on spinneret designs inherent in the integrated design, a modular quick-swap head shown in Figure A-4 was developed. The quick-swap head has no spinneret geometry, instead serving

as a foundation for modular plates with machined spinneret geometry to be quickly attached. This eliminates all of the machining steps required on the bulk of the head with every design iteration and allows the spinneret plates detailed in Section A.6 to be machined in a single fixture.

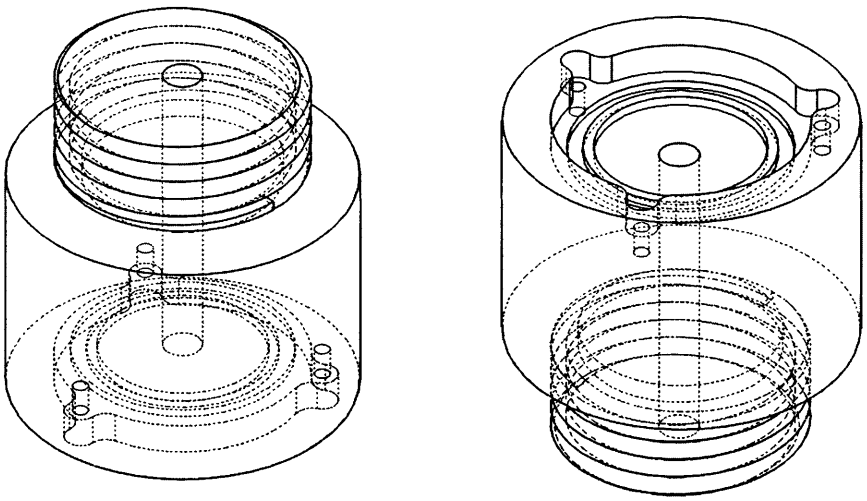

Figure A-4: Quick-swap head detail

A.5 Integrated Spinneret Receiver and Head Unit v2.0

The initial design for the quick-swap head and spinneret receiver were frequently subject to spills of polymer solution, and the large UNF 1-12 threads of the quick-swap head had a tendency to clog and jam with dried polymer. These issues were eliminated with the second generation of the receiver, which integrates both the receiver and quick-swap head into a single package, as can be seen in Figure A-5. This single unit is suspended atop the cantilevered support from the non-conductive stand via an acrylic plate. The integrated unit is connected to the plate via a pair of integrated ball plunger mechanisms which press ball bearings into a circumferential v-groove outer surface of the unit.

Figure A-5: Integrated second generation spinneret receiver and head unit detail

A.6 Quick-Swap Spinneret Plate

The various quick-swap spinneret plates, detailed in Figure A-6 were developed in conjunction with the quick-swap head as a faster alternative to iterating designs based on the unibody integrated spinneret head detailed in Section A.3. The plates were designed to be machined from 6.35mm (1/4in nominal) thick, 50.8mm (2in nominal) wide aluminum bar stock in a single machining setup without any re-fixturing. This design revision reduced the production time of a single spinneret by an order of magnitude to around 40 minutes of machining and encouraged a faster and more parallel design process.

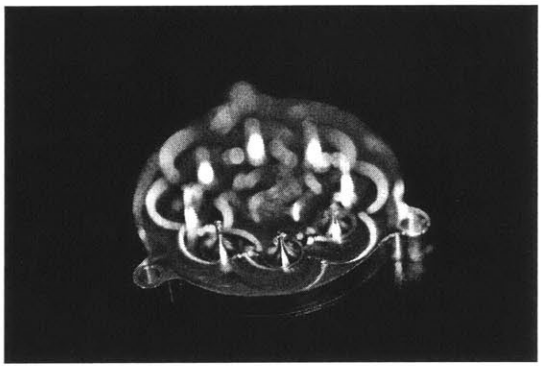

Figure A-6: Quick-swap spinneret plates detail

A.7 Air Entanglement Vortex

Since the individual spun fibers retain a surface charge after drying, they tend to repel each other. While this repulsion is directly responsible for the fibers whipping and lengthening, which greatly increases their surface area to volume ratio and causes massively increased drying, it also causes problems when the fibers reach the pill die cavity, which has a relatively small diameter compared to the diameter of the cylindrical spatial volume in which spinning occurs. To mediate fiber collection, an air entanglement vortex is used to force the fibers back together and into the pill die

cavity. This component is an aluminum block with a large 101.6mm (4in nominal) diameter hole in the center, with four tangentially aligned compressed air input ports, one per side of the block. The four compressed air ports allow a compressed air vortex to be created, creating additional entanglement and enhancing drying of the fibers.

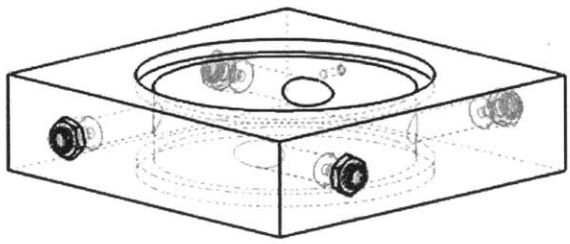

Figure A-7: Ancillary electrode and air entanglement vortex detail

A.8 Ancillary Electrodes

In the convective flow regime of the electrospinning process, the solvent has completely evaporated from the surface of the fibers, although a liquid core may still exist. When the flow regime transitions to this state, electric charge migrates to the surface of the fibers. The transition to this flow regime signals the onset of the 'bending instability' observed and characterized by [12]. At this point the fiber or fibers begin to self-repel in addition to continuing to repel other neighboring fibers. This combined with the ambient electric fields causes chaotic whipping of the fibers, which tend to spread out from the central axis. Ancillary copper ring electrodes were used to provide additional electric fields to counteract the interactions between the various fibers and drive the electrospun output into the pill die.

A.9 Die Floor Elevator

Initial experiments attempting to spin fibers into the die with minimal electromagnetic lensing discovered that the fibers repelled neighboring fibers enough to prevent deposition inside the die cavity when the die floor or ejector pin was located at the

bottom of the die. A device was built to provide the floor of the die with uniaxial translation, enabling travel of the floor the full height of the die, which is detailed in Figure A-9. The device is driven by a Minebea-Matsushita Corp. bipolar stepper motor (14PM-M201) driven by an EasyDriver stepper motor driver board. The stepper motor turns an 18-8 stainless steel 1/4"-16 Acme threaded rod. The mating Acme nut is press fit into the top of the device.

A.10 Die Punch and Post-Process Compaction

Following deposition of the electrospun material into the pill die cavity, the die can be moved transversely away from concentric alignment with the spinneret head in preparation for post-processing. A die punch can be brought down into the die, compressing the entangled fibers into a homogeneous tablet or pill. The punch head is manufactured in the negative of the top of the tablet or pill to be produced, as the ejector pin and die cavity floor was the negative of the bottom of said tablet. Figure 3-16 shows this process as a series of points in time over the course of one tablet compaction operation in a single pill die.

A.11 Die Cavity and Ejector Pin

In order to electrospin into a die cavity, the die itself must be electrically non-conductive, with only a small area in the center of the bottom of the die serving as a conductive, grounded collector. This is accomplished through the use of an electrically non-conductive die material, while the die ejector pin is composed of an electrically conductive material. The pin acts as a grounded collector but the rest of the die has no effect on the electric field lines and thus the spun fibers can be directed into the cavity effectively. This is observed in Figure A-10, which details the die cavity cross sections, where additionally, a second cavity design can be seen with a funnel-shaped entrance region. This feature may be used if initial designs run into issues inserting the fibers into the die and fibers instead collect on the outside top of

the die.

A.12 Nozzle Geometry and Flow

The geometry surrounding any orifice through which spinning solution exits can have a significant effect on subsequent jet formation especially if it results in preferential or limited wetting of the spinneret head. Varying nozzle geometry was studied including nozzles with comparable geometry to a syringe needle, as well as linear and curvilinear slots.

A.13 Droplet Formation

In support of the design of experiments on nozzle geometry, it was necessary to model the droplets formed at the orifice of each nozzle. The motivation came from the hypothesis that a nozzle which could suspend a larger droplet against gravitational, and eventually electrical, forces could support electrospinning of a larger jet, leading to higher production rates from each nozzle. As the electrospinning process ideally involves a steady state balance between mass flow into the droplet pumped from a reservoir of spinning solution and mass flow out of the droplet due to electrical forces spinning a jet, the geometry of stable droplets hanging from each nozzle tip was of interest. A simplified model of these drops can be found in the equation describing axially-symmetric sessile and pendant droplets of fluid which rest on, or hang from, a homogeneous surface respectively. The equation governing the geometry of these drops was developed by Bashforth and Adams [1] and is presented in (A.1).

$$\gamma(\frac{\sin\phi}{x} + \frac{1}{R_1}) = \frac{2\gamma}{b} + \Delta g z \tag{A.1}$$

The various parameters in the Bashforth-Adams equation (A.1) are described in Figure A-11 which overlays them on a cross section of sessile drop. Note that the parameter b, which is not shown, is the radius of curvature of the drop surface at the apex of the drop, location O.

For a droplet hanging upon a nozzle with a circular cross-section with zero flow and zero electric charge, the planar face of the nozzle can be approximated as an unbroken plane and the orifice itself can be assumed to have no effect on the droplet size, since the liquid surface tension and the surface energy of the material composing the nozzle govern the droplet geometry. Thus the Bashforth-Adams equation can be used as an accurate approximation of the uncharged droplet geometry on the nozzle head. Furthermore, since the assumption is a zero flow situation, the geometry of the orifice itself is insignificant. This means that as long as the the planar face of the nozzle is circular, the Bashforth-Adams equation (A.1) is valid as an approximation

A.14 Needle Arrays

Previous studies have sought to characterize optimal arrangements of multi-needle setups. Yang *et al.* found that the densest planar needle arrangement occurred when a needle was located at each corner of an equilateral triangle, if those triangles were further arranged in equilateral hexagons, and this pattern repeated to fill the plane [11].

A.15 Contact Angles

The contact angles of the various spinning solutions used in testing were measured using a contact angle goniometer. The measurements were made under similar conditions to actual experiment conditions; solution droplets were deposited upon a clean, flat machined aluminum 6061 surface at room temperature in an atmospheric gaseous environment. This sessile drop technique was used to measure the advancing contact angle, as a sessile drop was deposited by pipette. An example contact angle for a PVP solution used in the experiments is found in Figure A-12

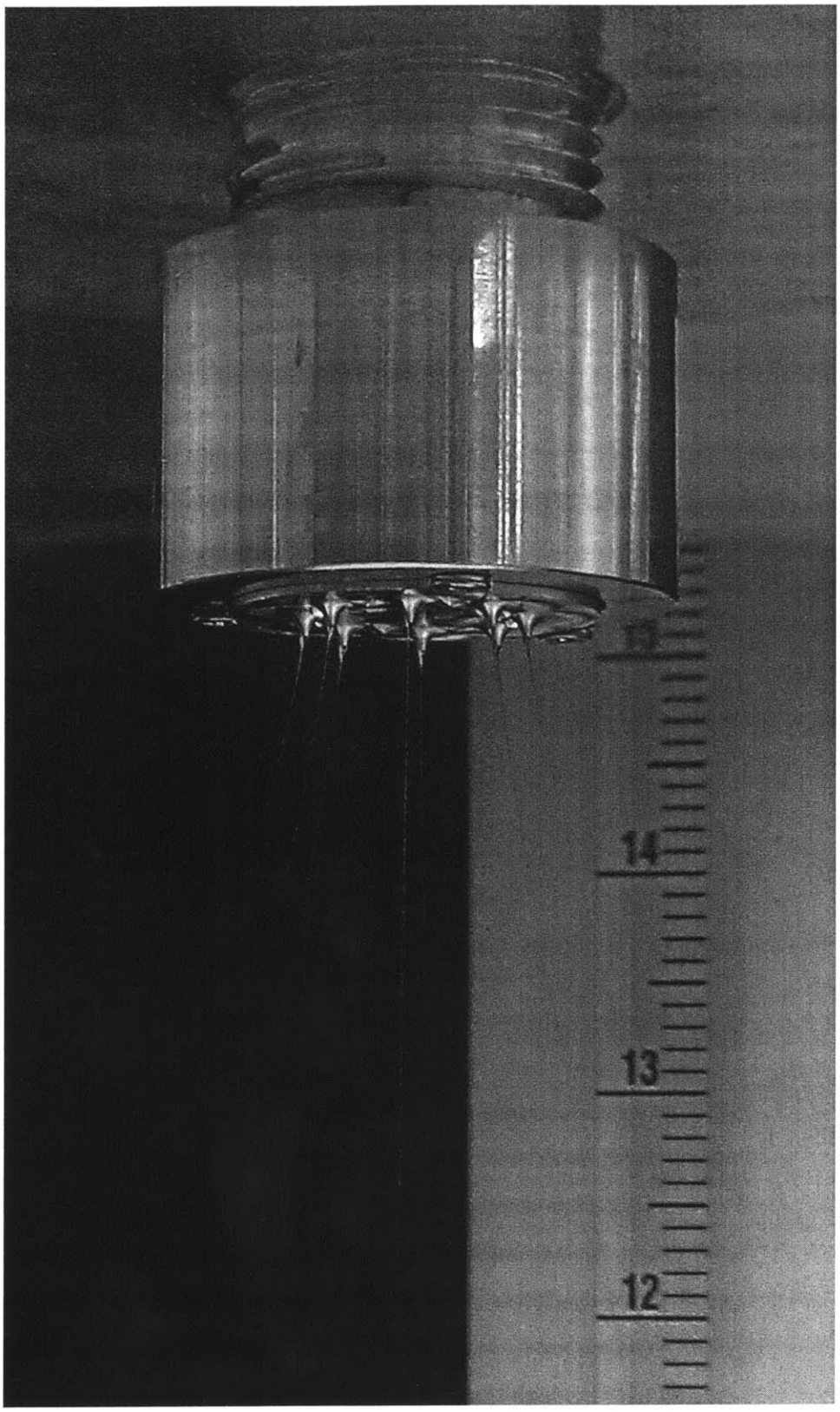

Figure A-8: Quickswap head detail

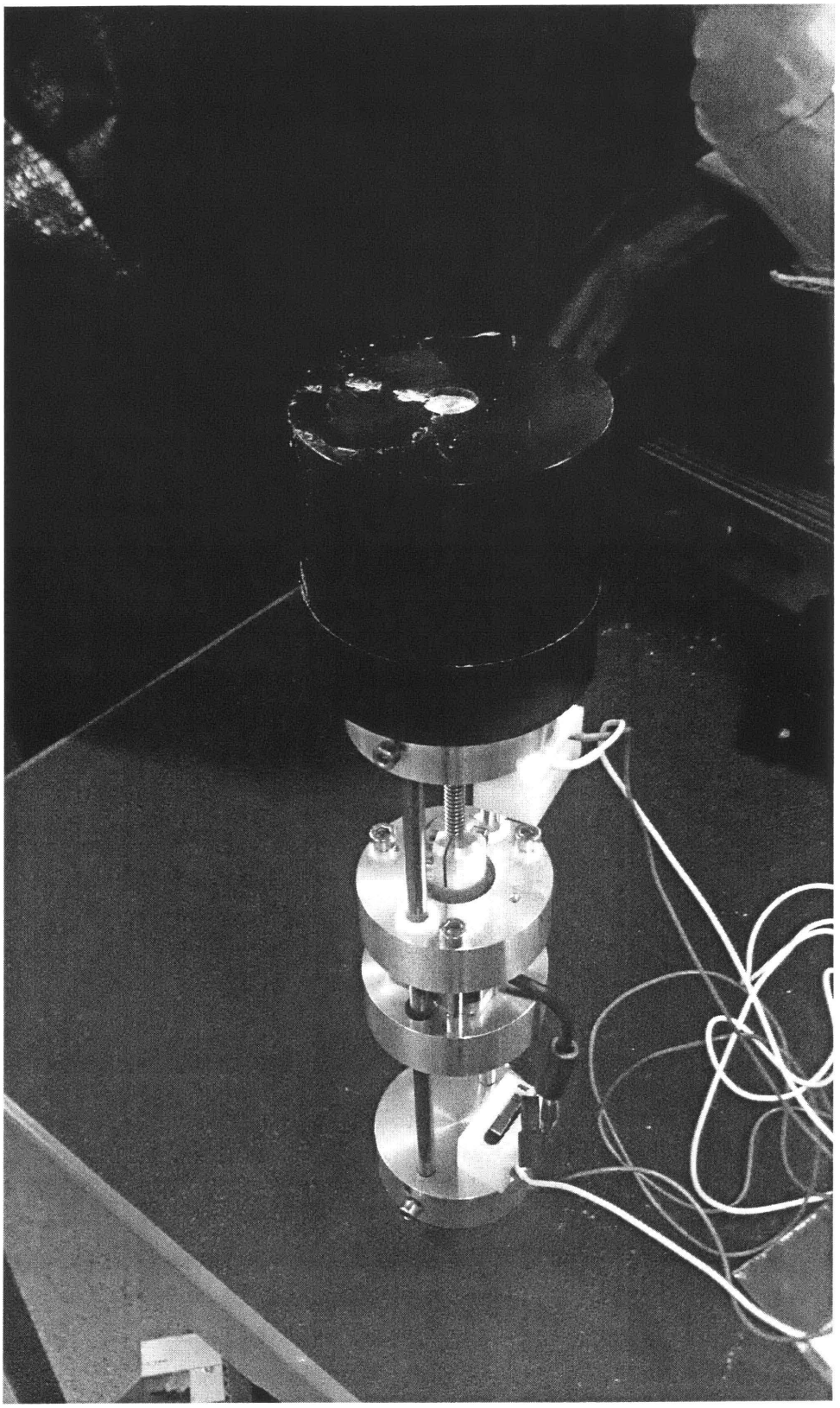

Figure A-9: Mechanism for retraction of die floor detail

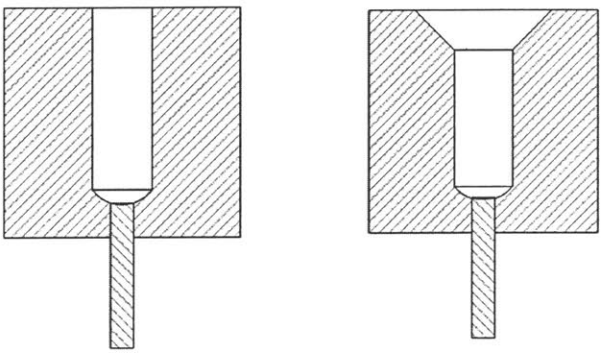

Figure A-10: Ancillary electrode and air entanglement vortex detail

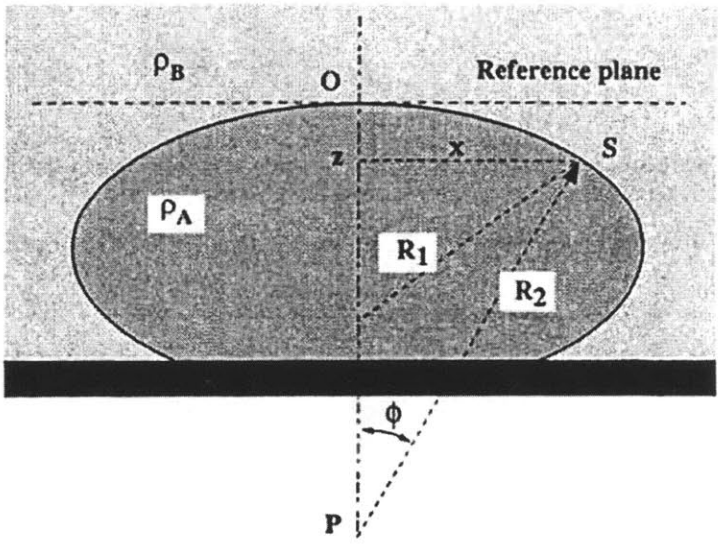

Figure A-11: Parameters of Bashforth-Adams equation on a cross-section of a sessile drop [1]

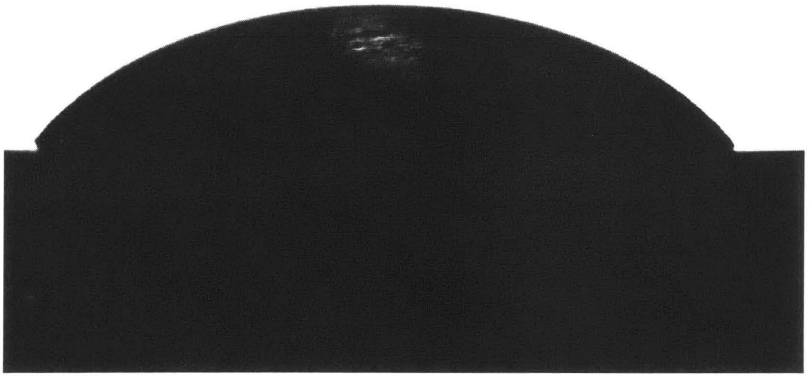

Figure A-12: Example sessile drop picture taken with goniometer; 8 wt% 1.3MDa PVP and ethanol solution

THIS PAGE INTENTIONALLY LEFT BLANK

Appendix B

Electrostatic Field Modeling

B.1 Finite Element Solver Code

```
% ------------------------------------------------------------------------
% MIT-Novartis Center for Continuous Manufacturing
% Electrospinning Rig Electric Field Simulation

% Written by:
% Nicholas Matti Sondej
% Precision Engineering Research Group
% v1.0 4/5/2013

% ------------------------------------------------------------------------

function [matrix] = electric_field_simulation()
% Simulate electric fields generated by charged spinneret and grounded
% collector
% Note: fields simulated from r = 0 to r = R, then mirrored for graph

% Size of physical area
dim_r = 0.3; % [m]
dim_z = 0.22; % [m]
```

```
% Size of node array
npts_r = 40;
npts_z = round(npts_r * dim_z/dim_r);

% Differentials
dr = dim_r/npts_r;
dz = dim_z/npts_z;

% Experiment parameters
v_spin = 35; % [kV]
v_col = 0; % [kV]
v_anc1 = 35; % [kV]
v_anc2 = 30; % [kV]
v_anc3 = 20; % [kV]

% Spinneret parameters
r_spinneret = 0.0125; % [m]
%r_receiver = 0.1524; % [m] Current conditions
r_receiver = 0.02; % [m]
z_spinneret = 0.022; % [m]

% Spinneret node boundaries
r_spin_nodes = ceil(r_spinneret/dr);
r_rec_nodes = ceil(r_receiver/dr);
z_spin_nodes = ceil(z_spinneret/dz);

% Collector parameters - CHANGE THIS FOR DIFFERENT EFFECTS
r_collector = 0.001; % [m]

% Collector node boundaries
r_col_nodes = ceil(r_collector/dr);

% Ancillary electrode parameters
r_ancillary = 0.75; % [m]
z_ancillary = 0.05; % [m]
r_anc = 0.005; % [m] Ring electrode radius
```

```
r_ancillary2 = 0.075; % [m]
z_ancillary2 = 0.125; % [m]
r_anc2 = 0.005; % [m] Ring electrode radius

r_ancillary3 = 0.05; % [m]
z_ancillary3 = 0.175; % [m]
r_anc3 = 0.005; % [m] Ring electrode radius


% Ancillary electrode centers
r_anc_node = ceil(r_ancillary/dr);
z_anc_node = ceil(z_ancillary/dz);

r_anc_node2 = ceil(r_ancillary2/dr);
z_anc_node2 = ceil(z_ancillary2/dz);

r_anc_node3 = ceil(r_ancillary3/dr);
z_anc_node3 = ceil(z_ancillary3/dz);

% Matrix setup
coeffs = zeros(npts_z*npts_r, npts_z*npts_r);
C = zeros(npts_z*npts_r,1);

for z = 1:npts_z
    for r = 1:npts_r
        % Note: since indexes start at 1, for linearized arrays, must
        % subtract 1 from rows before multiplying by npts_z

        % Deal with internal spinneret points
        if (z < z_spin_nodes) && (r < r_spin_nodes)
            temp = zeros(1,npts_z*npts_r);
            temp((z-1)*npts_r + r) = 1;
            coeffs((z-1)*npts_r + r, :) = temp;
            C((z-1)*npts_r +r, 1) = v_spin;
```

```
% Type 1
elseif (z == z_spin_nodes) && (r == 1)
    temp = zeros(1,npts_z*npts_r);
    temp((z-1)*npts_r + r) = 1;
    coeffs((z-1)*npts_r + r, :) = temp;
    C((z-1)*npts_r +r, 1) = v_spin;

% Type 2
elseif (z == z_spin_nodes) && (r < r_spin_nodes)
    temp = zeros(1,npts_z*npts_r);
    temp((z-1)*npts_r + r) = 1;
    coeffs((z-1)*npts_r + r, :) = temp;
    C((z-1)*npts_r +r, 1) = v_spin;

% Type 3
elseif (z == z_spin_nodes) && (r == r_spin_nodes)
    temp = zeros(1,npts_z*npts_r);
    temp((z-1)*npts_r + r) = 1;
    coeffs((z-1)*npts_r + r, :) = temp;
    C((z-1)*npts_r +r, 1) = v_spin;

% Type 4
elseif (z < z_spin_nodes) && (r == r_spin_nodes)
    temp = zeros(1,npts_z*npts_r);
    temp((z-1)*npts_r + r) = 1;
    coeffs((z-1)*npts_r + r, :) = temp;
    C((z-1)*npts_r +r, 1) = v_spin;

% Type 5
elseif (z == 1) && (r == r_spin_nodes)
    temp = zeros(1,npts_z*npts_r);
    temp((z-1)*npts_r + r) = 1;
    coeffs((z-1)*npts_r + r, :) = temp;
    C((z-1)*npts_r +r, 1) = v_spin;

% Type 6
```

```
elseif (z == 1) && (r > r_spin_nodes) && (r < r_rec_nodes)
    temp = zeros(1,npts_z*npts_r);
    temp((z-1)*npts_r + r) = 1;
    coeffs((z-1)*npts_r + r, :) = temp;
    C((z-1)*npts_r +r, 1) = v_spin;

% Type 7
elseif (z == 1) && (r == r_rec_nodes)
    temp = zeros(1,npts_z*npts_r);
    temp((z-1)*npts_r + r) = 1;
    coeffs((z-1)*npts_r + r, :) = temp;
    C((z-1)*npts_r +r, 1) = v_spin;

% Type 8
elseif (z == 1) && (r > r_rec_nodes)
    temp = zeros(1,npts_z*npts_r);
    temp((z-1)*npts_r + (r-1)) = dz;
    temp((z-1)*npts_r + (r+1)) = dz;
    % Extra factor to give correct BCs at edge to prevent corner
    % insulation
    temp(z*npts_r + r) = dr*((npts_r -r)/npts_r + r/(2*npts_r));
    temp((z-1)*npts_r + r) = -(2*dz + dr);
    coeffs((z-1)*npts_r + r, :) = temp;
    C((z-1)*npts_r +r, 1) = 0;

% Type 9
elseif (z == 1) && (r == npts_r)
    temp = zeros(1,npts_z*npts_r);
    temp((z-1)*npts_r + (r-1)) = dz;
    temp(z*npts_r + r) = dr;
    temp((z-1)*npts_r + r) = -(dz + dr);
    coeffs((z-1)*npts_r + r, :) = temp;
    C((z-1)*npts_r +r, 1) = 0;

%       % Type 10
%       elseif (r == npts_r) && (z > 1) && (z < npts_z)
```

```
%             temp = zeros(1,npts_z*npts_r);
%             temp((z-2)*npts_r + r) = dr;
%             % Extra factor to give correct BCs at edge to prevent corner
%             % insulation
%             temp((z-1)*npts_r + (r-1)) = dz*((npts_z -z)/npts_z + z/(2*npts_z));
%             temp(z*npts_r + r) = dr;
%             temp((z-1)*npts_r + r) = -(2*dr + dz);
%             coeffs((z-1)*npts_r + r, :) = temp;
%             C((z-1)*npts_r +r, 1) = 0;

        % If setting walls to ground/v_spin
        % Type 10
        elseif (r == npts_r) && (z > 1) && (z < npts_z)
            temp = zeros(1,npts_z*npts_r);
            temp((z-1)*npts_r + r) = 1;
            coeffs((z-1)*npts_r + r, :) = temp;
            % Grounded Walls
            C((z-1)*npts_r +r, 1) = 0;
            % Charged Walls
%             C((z-1)*npts_r +r, 1) = v_spin;

        % Type 11
        elseif (z == npts_z) && (r == npts_r)
            temp = zeros(1,npts_z*npts_r);
            temp((z-2)*npts_r + r) = dr;
            temp((z-1)*npts_r + (r-1)) = dz;
            temp((z-1)*npts_r + r) = -(dz + dr);
            coeffs((z-1)*npts_r + r, :) = temp;
            C((z-1)*npts_r +r, 1) = 0;

        % Type 12
        elseif (z == npts_z) && (r > r_col_nodes)
            temp = zeros(1,npts_z*npts_r);
            temp((z-2)*npts_r + r) = dr;
            temp((z-1)*npts_r + (r-1)) = dz;
            temp((z-1)*npts_r + (r+1)) = dz;
```

```
    temp((z-1)*npts_r + r) = -(dr + 2*dz);
    coeffs((z-1)*npts_r + r, :) = temp;
    C((z-1)*npts_r +r, 1) = 0;

% Type 13
elseif (z == npts_z) && (r == r_col_nodes)
    temp = zeros(1,npts_z*npts_r);
    temp((z-1)*npts_r + r) = 1;
    coeffs((z-1)*npts_r + r, :) = temp;
    C((z-1)*npts_r +r, 1) = v_col;

% Type 14
elseif (z == npts_z) && (r > 1) && (r < r_col_nodes)
    temp = zeros(1,npts_z*npts_r);
    temp((z-1)*npts_r + r) = 1;
    coeffs((z-1)*npts_r + r, :) = temp;
    C((z-1)*npts_r +r, 1) = v_col;

% Type 15
elseif (z == npts_z) && (r == 1)
    temp = zeros(1,npts_z*npts_r);
    temp((z-1)*npts_r + r) = 1;
    coeffs((z-1)*npts_r + r, :) = temp;
    C((z-1)*npts_r +r, 1) = v_col;

% Type 16
elseif (r == 1)
    temp = zeros(1,npts_z*npts_r);
    temp((z-2)*npts_r + r) = dr;
    temp((z-1)*npts_r + (r+1)) = dz;
    temp(z*npts_r + r) = dr;
    temp((z-1)*npts_r + r) = -(dz + 2*dr);
    coeffs((z-1)*npts_r + r, :) = temp;
    C((z-1)*npts_r +r, 1) = 0;

%       % Ancillary electrode 1 modeled as circle
```

```
%         elseif (z*dz - z_anc_node*dz)^2 + (r*dr - r_anc_node*dr)^2 <= r_anc^2
%
%             temp = zeros(1,npts_z*npts_r);
%             temp((z-1)*npts_r + r) = 1;
%             coeffs((z-1)*npts_r + r, :) = temp;
%             C((z-1)*npts_r +r, 1) = v_anc1;
%         elseif (z*dz - z_anc_node2*dz)^2 + (r*dr - r_anc_node2*dr)^2 <= r_anc2^2
%
%             temp = zeros(1,npts_z*npts_r);
%             temp((z-1)*npts_r + r) = 1;
%             coeffs((z-1)*npts_r + r, :) = temp;
%             C((z-1)*npts_r +r, 1) = v_anc2;
%         elseif (z*dz - z_anc_node3*dz)^2 + (r*dr - r_anc_node3*dr)^2 <= r_anc3^2
%
%             temp = zeros(1,npts_z*npts_r);
%             temp((z-1)*npts_r + r) = 1;
%             coeffs((z-1)*npts_r + r, :) = temp;
%             C((z-1)*npts_r +r, 1) = v_anc3;
%         % Secondary electrode
%         elseif (z == z_anc_node2) && (r == r_anc_node2)
%             temp = zeros(1,npts_z*npts_r);
%             temp((z-1)*npts_r + r) = 1;
%             coeffs((z-1)*npts_r + r, :) = temp;
%             C((z-1)*npts_r +r, 1) = v_anc;
%
        % All interior points
        else
            temp = zeros(1,npts_z*npts_r);
            temp((z-2)*npts_r + r) = dr;
            temp((z-1)*npts_r + (r+1)) = dz;
            temp(z*npts_r + r) = dr;
            temp((z-1)*npts_r + (r-1)) = dz;
            temp((z-1)*npts_r + r) = -(2*dz + 2*dr);
            coeffs((z-1)*npts_r + r, :) = temp;
            C((z-1)*npts_r +r, 1) = 0;
        end
```

```
    end
end

temp = coeffs\C;
temp = temp';

matrix = zeros(npts_z, npts_r);

for i = 1:npts_z
    matrix(i,:) = temp((i-1)*npts_r + 1: i*npts_r);
end
c_line = matrix(:,1)';

% figure()
% plot(c_line);

temp = matrix(:,end:-1:1);
matrix = [temp matrix];
cplots(matrix, npts_z, npts_r, dim_z, dim_r);
hold on
fieldlines(matrix,dim_z,dim_r,dz,dr)
end

function fieldlines(matrix,dim_z,dim_r,dz,dr)
[Z, R] = size(matrix);
u = zeros(Z-2, R-2);
v = zeros(Z-2, R-2);

for z = 2:Z-1
    for r = 2:R-1
        v(z-1,r-1) = (matrix(z-1,r) - matrix(z+1,r))/(2*dz);
        % Need to figure out the following below: why does r not need to be
        % negative?
        u(z-1,r-1) = (matrix(z,r-1) - matrix(z,r+1))/(2*dr);
    end
end
```

```
zgv = dim_z - dz:-dz:0;
rgv = -dim_r:dr:dim_r - dr;
[R, Z] = meshgrid(rgv, zgv);

u = u(end:-1:1,:);
v = v(end:-1:1,:);

% Normalize vectors so arrows are readable
% n = sqrt(u.^2 + v.^2);
% u = u./n;
% v = v./n;

figure()
quiver(R(2:end-1,2:end-1),Z(2:end-1,2:end-1),u,v,3)
axis equal
xlabel('Radial Distance from Axial Centerline [m]');
ylabel('Axial Distance from Spinneret Head [m]');
axis ij
end

function cplots(matrix, npts_z, npts_r, dim_z, dim_r)
dz = dim_z/npts_z;
dr = dim_r/npts_r;

zgv = dim_z - dz:-dz:0;
rgv = -dim_r:dr:dim_r - dr;

[R, Z] = meshgrid(rgv, zgv);
%
%
% Z_mir = Z(:,end:-1:1);
% Z = [Z_mir Z];
% R_mir = R(:,end:-1:1) .* -1;
% R = [R_mir R];
```

```
matrix = matrix(end:-1:1,:);
b = figure();
[C,handle] = contour(R,Z,matrix,60);
xlabel('Radial Distance from Axial Centerline [m]');
ylabel('Axial Distance from Spinneret Head [m]');
axis ij
axis equal
c_bar = colorbar();
set(get(c_bar,'ylabel'),'String','Electrostatic Potential [kV]');
% set(handle,'LineColor','none');
% get(gca,'XTick')
% set(gca,'XTick',xtick(2:end));
% set(gca,'YTick',ytick(2:end));
% set(gca,'XTickLabel',xtick1(2:end));
% set(gca,'YTickLabel',ytick1(2:end));
% get(gca,'XTick');
% title(t);
% xlabel('Distance from Vertical Centerline (m)');
% ylabel('Distance from Horizontal Centerline (m)');

% saveas(b, ['contourmap_hy_' num2str(h)],'jpg');
end
```

THIS PAGE INTENTIONALLY LEFT BLANK

Appendix C

Electrostatic Lensing

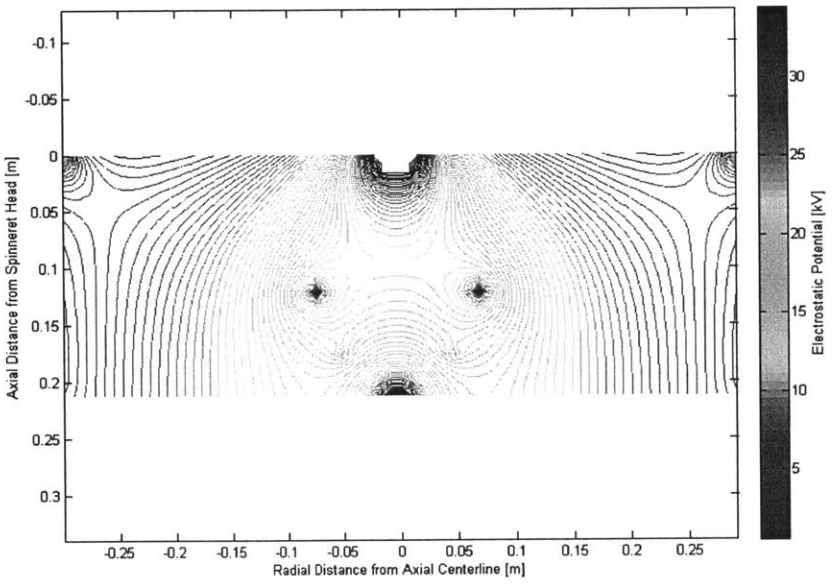

Figure C-1: Finite difference model of system with ancillary electrodes

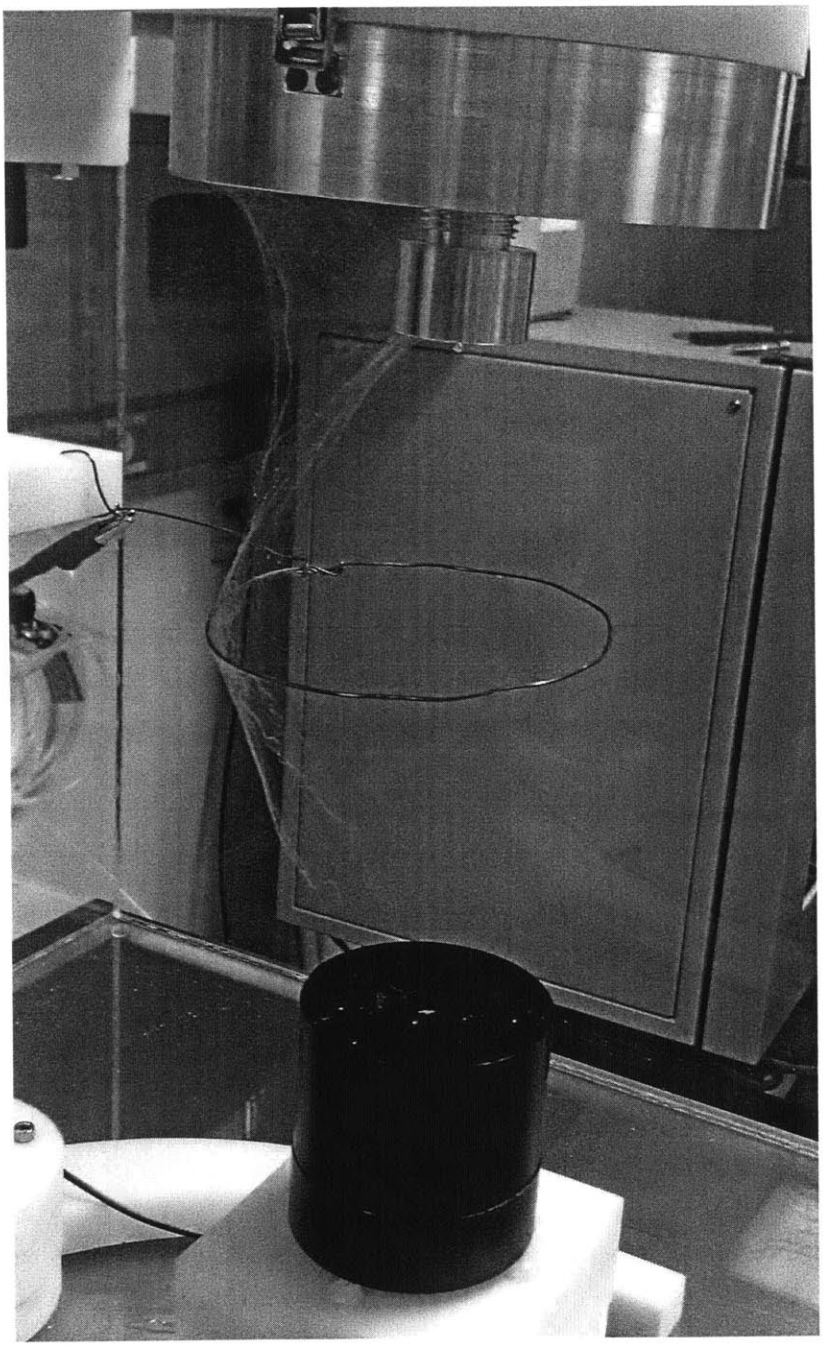

Figure C-2: Spinning results on ancillary electrodes

Appendix D

Manufacturing Process Development Work

	Value	Unit
Solution Characteristics		
Solution density	1	g/mL
API density	0.789	g/mL
API weight %	8.0%	wt%
Pill Characteristics		
Pill mass	0.3	g/pill
Process Characteristics		
Annual production rate	1000000000	pills/yr
Weekly uptime/year	50	wk/yr
Daily uptime/week	7	day/wk
Hourly uptime/day	24	hr/day
Hours/year uptime	8400	hr/yr
Pill production rate	119047.6	pills/hr
	1984.1	pills/min
	33.1	pills/sec
Process API mass output rate	35714.3	g/hr
	35.7	kg/hr
	595.2	g/min
Process API volumetric output	595.2	mL/min
Process solution volumetric output*	7440.5	mL/min

Figure D-1: Process Calculations

```
% ------------------------------------------------------------------------
% MIT-Novartis Center for Continuous Manufacturing
% Spatially-Constrained Electrospinning Pill Manufacturing Model

% Written by:
% Nicholas Matti Sondej
% Precision Engineering Research Group
% v1.0 2/27/2013

%------------------------------------------------------------------------


% function [pill_prod_time] = pill_production(v_flowrate, rho_api, rho_polymer, rho_solv
clc
clear

% Material Constants
rho_api = 1.085;     % Ibuprofen [g/cm^3]
rho_polymer = 1.18; % Polyvinylpyrrolidone [g/cm^3]
rho_solvent = 0.785; % Ethanol [g/cm^3]

% Solution Constants
api_wt_per = 0.08;
polymer_wt_per = 0.08;
solvent_wt_per = 1 - api_wt_per - polymer_wt_per;

% Process Constants
V_flowrate_module = 0.5; % [ml/min]
api_production_goal = 595; % [g/min] 1B pill/year
pill_mass = 0.3; % [g]


num_modules = [];
z = [];

for j = 1:100
```

```
num_modules = [num_modules j];
flowrate = [];
api_prod_rate = [];
n_modules_depend = [];
for i = 0.5:0.05:5
V_flowrate_module = i;
flowrate = [flowrate i];
% until you find a better way to this use:
rho_solution = 1/(api_wt_per/rho_api + polymer_wt_per/rho_polymer + solvent_wt_per/

api_vfrac = api_wt_per * rho_solution / rho_api;
polymer_vfrac = polymer_wt_per * rho_solution / rho_polymer;
solvent_vfrac = solvent_wt_per * rho_solution / rho_solvent;

% Check to see volume fractions add to 1
if(api_vfrac + polymer_vfrac + solvent_vfrac == 1)
    display('Volume Fractions Valid')
else
    display('Invalid Volume Fractions')
end

V_flowrate_api = V_flowrate_module * api_vfrac; % [ml/min]
V_flowrate_polymer = V_flowrate_module * polymer_vfrac; % [ml/min]
V_flowrate_solvent = V_flowrate_module * solvent_vfrac; % [ml/min]

V_flowrate_solids = V_flowrate_api + V_flowrate_polymer; % [ml/min]

m_flowrate_api = V_flowrate_api * rho_api; % [g/min]
m_flowrate_polymer = V_flowrate_polymer * rho_polymer; % [g/min]
m_flowrate_solvent = V_flowrate_solvent * rho_solvent; % [g/min]

m_flowrate_solids = m_flowrate_api + m_flowrate_polymer; % [g/min]

pill_production_time = pill_mass / m_flowrate_api; % [min]
module_production_rate = 60/pill_production_time; % [pills/hr]
%num_modules = api_production_goal / m_flowrate_api; % [modules]
```

```
    api_prod_rate = [api_prod_rate m_flowrate_api];
    n_modules_depend = [n_modules_depend (api_production_goal / (V_flowrate_module * ap
    end
    z = [z; api_prod_rate*j*60];
end

figure();
surf(flowrate, num_modules, z);

xlabel('Flowrate [ml/min]');
ylabel('Number of Modules');
zlabel('API Production Rate [g/hr]')

display('Pill unit production time:')
display(pill_production_time)

display('Module hourly production rate:')
display(module_production_rate)

display('Number of modules needed:')
display(num_modules)

figure();
plot(flowrate, n_modules_depend,'r');
xlabel('Flowrate [ml/min]');
ylabel('Number of Modules');
```

Bibliography

[1] Francis Bashforth and John Couch Adams. An attempt to test the theories of capillary action, 1883.

[2] Blair Kathryn Brettmann. Electrospinning for pharmaceutical applications. 2012.

[3] J. M. Deitzel, J. Kleinmeye, D. Harris, and N. C. Beck Tan. The effect of processing variables on the morphology of electrospun nanofibers and textiles. *Polymer*, 42:12, 2001.

[4] Alice Hong. The dielectric strength of air, 2000.

[5] P. Katta, M. Allesandro, R. D. Ramsier, and G. G. Chase. Continuous electrospinning of aligned polymer nanofibers onto a wire drum collector. *Nano Letters*, 4(11):4, 2004.

[6] Alcoa Engineered Products. Alloy 6061: Understanding extruded aluminum alloys. 2002.

[7] Y.M. Shin, M.M. Hohman, M.P. Brenner, and G.C. Rutledge. Experimental characterization of electrospinning: the electrically forced jet and instabilities. *Polymer*, 42:18, 2001.

[8] Thandavamoorthy Subbiah, G. S. Bhat, R. W. Tock, S. Parameswaran, and S. S. Ramkumar. Electrospinning of nanofibers. *Journal of Applied Polymer Science*, 96(2):13, 2004.

[9] Geoffrey Taylor. Electrically driven jets. *Proceedings of the Royal Society of London. A. Mathematical and Physical Sciences*, 313(1515):453–475, 1969.

[10] S. A. Theron, A. L. Yarin, E. Zussman, and E. Kroll. Multiple jets in electrospinning: experiment and modeling. *Polymer*, 46(9):2889–2899, 2005.

[11] Ying Yang, Zhidong Jia, Qiang Li, Lei Hou, Jianan Liu, Liming Wang, Zhicheng Guan, and Markus Zahn. A shield ring enhanced equilateral hexagon distributed multi-needle electrospinning spinneret. *IEEE Transactions on Dielectrics and Electrical Insulation*, 17(5):1592–1601, 2010.

[12] A. L. Yarin, S. Koombhongse, and D. H. Reneker. Bending instability in electrospinning of nanofibers. *Journal of Applied Physics*, 89(5), 2001.